# A Transition Radiation Detector and Gas Supply System for AMS

by

Bilge Melahat Demirköz

Submitted to the Department of Physics
in partial fulfillment of the requirements for the degree of

Master of Science

at the

MASSACHUSETTS INSTITUTE OF TECHNOLOGY

May 2004



Author .....
Department of Physics
May 7, 2004

Certified by .....
Ulrich J. Becker
Professor of Physics
Thesis Supervisor

Accepted by .....
Thomas Greytak
Chairman, Department Committee on Graduate Students

# A Transition Radiation Detector and Gas Supply System for AMS

by

Bilge Melahat Demirköz

Submitted to the Department of Physics
on May 7, 2004, in partial fulfillment of the
requirements for the degree of
Master of Science

## Abstract

Alpha Magnetic Spectrometer is an experiment that will be on the International Space Station for three years. It will look for anti-matter and dark matter. Supersymmetric dark matter could produce an excess in the 10-300GeV positron spectrum. A $10^{-6}$ separation of positrons from the more abundant protons is planned for this signal. A TRD (Transition Radiation Detector) has been designed to achieve these physics goals. Besides the radiator, the TRD is a gaseous detector that needs a gas system providing signal stability to 3%. The design, and construction of the TRD gas supply system is described with emphasis on the electronics control.

Thesis Supervisor: Ulrich J. Becker
Title: Professor of Physics

# Acknowledgments

I am very appreciative of all my teachers' dedication to the education of their students. In particular, I have greatly benefitted from Prof. Ulrich Becker's wisdom, extensive experience and great depth of knowledge. I would like to thank him for exposing me to the particle physics community and giving me the tools to continue my career. I would also like to thank Prof. Kate Scholberg for her unfaltering enthusiasm and incredible kindness. My special thanks extends to Prof. Peter Fisher for useful discussions and for continuing to guide me and to offer me practical advice.

I would also like to thank Prof. Ting who made AMS possible and for giving me the chance to work on this project. In the past four years, it has been my pleasure to work together with Reyco Henning, Gianpaolo Carosi, Ben Monreal, Sa Xiao, Gray Rybka, Yoshi Uchida, Dafne Baldassari, Andrew Werner, Shi Yue, Teresa Fazio, Josh Thompson, Blake Stacey, Kasey Ensslin and Grant Elliott. Elvio Sadun's and Wang Yi's dedication to GP:50 component testing is greatly appreciated. My discussions with Alex Shirokov were very valuable. As for Christine Titus and Mike Grossman, I do not know how I could survive without them.

I have learned a lot from Alexei Lebedev, Alessandro Bartoloni, Vladimir Koutsenko and Hans-Bernhard Bröker who helped with the electronics and slow control programming. I would like to thank Joe Burger, Peter Berges, Robert Becker and Maurice Vergain for their help and support during the engineering Box S integration at CERN as well as other AMS collaborators, including Georg Schwering, Thorsten Siedenburg, Thomas Kirn, Mike Capell, Nichelle Wood and Simonetta Gentile.

I would like to thank Profs. Aron Bernstein, Dick Yamamoto, Dave Pritchard, Washington Taylor and Bolek Wyslouch for their valuable advice and guidance. I am also greatly indebted to Dr. Scott Sewell, Dr. Jay Kirsch and Nancy Savioli for believing in me, even when I did not.

Needless to say, none of this would be possible without the support of my family and friends; I can not thank them enough.

# Contents

# List of Figures

# List of Tables

# Chapter 1

# Introduction

This thesis addresses three necessarily closely related topics:

1. The experimental quest to study high energy positrons from space for the first time over a wide energy range. These studies include a possible insight into the nature of "Dark Matter."

2. The design and the realization of a Transition Radiation Detector (TRD) in space for ultra-relativistic charged cosmics as part of the AMS experiment, considering that a TRD on earth is a difficult detector.

3. The painstaking technical details needed for the accuracy and realization of the detector which are documented for NASA traceability in future years.

My involvement started with the optimization and performance studies of the TRD and continued with the design, construction and electronics control of the TRD gas system.

AMS is a magnetic spectrometer which measures the momentum, the charge, the velocity and the energy of a particle using a super-conducting magnet and complimentary detectors, shown in Fig. 1-1. Reconstructing the particle's curvature in the magnetic field of AMS allows for the measurement of momentum and charge of the particle. AMS has been designed to allow for cross-checks between measurements from different detectors. AMS can measure the momentum of particles up to

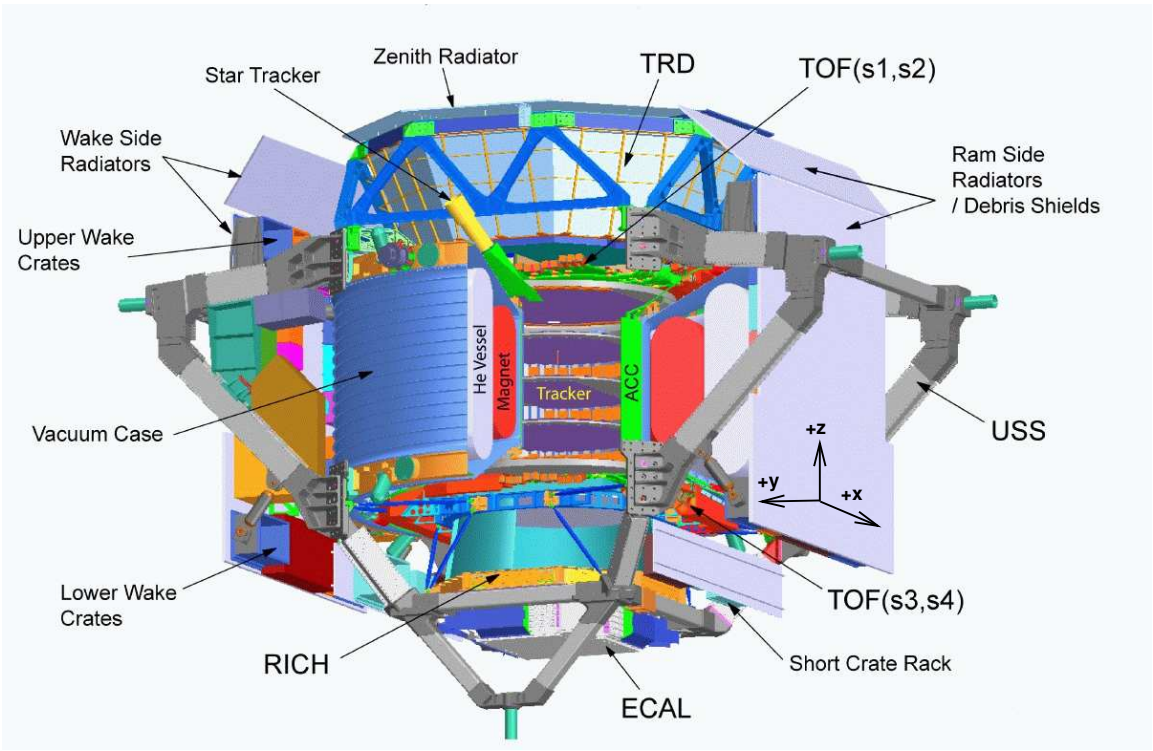


Figure 1-1: The AMS detector

3 TeV/nucleon. High energy gamma rays which convert to $e^+e^-$ in the detector can also be identified and their energy determined.

The main physics goals are to look for anti-matter and dark matter. SUSY (Supersymmetric) dark matter could produce an excess in the $10 - 300$ GeV positron spectrum. A Transition Radiation Detector (TRD) is crucial in making this measurement because it separates positrons from the more abundant protons in this momentum range.

In a TRD, transition radiation (TR) is emitted when a relativistic particle moves across an interface of two media with different dielectric constants, [60]. The media in our case are a TR "radiator" and vacuum. Due to properties of the radiator and the other materials in the detector, the emitted radiation becomes appreciable when the Lorentz factor of the particle is greater than 1000. The radiation that is detected is in the X-ray region of the spectrum (1-30 keV). The total energy loss includes the ionization losses of the charged particle. The TRD is the only detector identifying

ultra-relativistic particles. Though the number of quanta released at each interface is low, one uses multiple layered radiators to increase this effect. This radiation is detected using proportional high-Z gas drift tubes. The radiation ionizes the gas mixture in the straw drift tube and the pulse of electrons is amplified. This pulse is proportional to the energy deposited in the tube by the particles. The AMS TRD consists of 20mm thick layers of fleece radiator material and 6mm proportional straw tubes filled with Xe:$CO_2$=80:20 gas operated at an avalanche gain of $\approx 3000$. With 20 layers, a rejection factor of $10^{-2}$-$10^{-3}$ of protons from positrons can be expected. The rejection achieved is highly dependent on a constant signal height of the proportional tubes. The avalanche gain is a strong function of the mixing accuracy and of the temperature, which varies about $100^o$ in space. Diffusion through the straw foils is different for Xenon and $CO_2$ and must be balanced. Therefore the rejection critically depends on the accuracy of the gas supply system, keeping the ratio constant.

This thesis focuses on the design and construction of the TRD and its gas supply system. The gaseous volume of the TRD is 230 liters and it will slowly be leaking into space. To replenish the system and keep the pressure in the active volume of the TRD at 1.2 atmosphere in space, a gas system is needed. The system comprises of a module for supply, one for circulation, and manifolds for distribution. These subsystems will each be under the control of dedicated and redundant electronics cards. An automated mixing program will premix Xenon and $CO_2$ gases to the necessary proportion using the law of partial pressures. A series of high pressure valves and pressure sensors in the supply unit will mix the gas into a buffer volume. About 50 kg of Xenon and 5 kg of $CO_2$ are needed for the full mission. A maximum of 7 liters will be transfered from the buffer to the TRD every day, in a mixture compensating for the different losses of Xe and $CO_2$.

The space environment and limited remote control via satellite to the Space Station has influenced several design decisions in AMS. All detector subsystems and electronics have to be space qualified; for instance, they have to withstand vibration tests and be radiation hard. All components also have to function under the fringe field of the 0.86 Tesla AMS magnet. AMS has to operate under different temperature

conditions as well: from -20 to 65$^o$C. To this end, components of the TRD gas system have been tested extensively. Also, besides the flight gas system, an engineering flight system has been constructed to test out reliability and verify each control command before being sent to the ISS. The slow control of the gas system has been tested out using a test-design system at MIT. Using the flight communication protocols between the cards and the subsystems, a simple mixing program can mix argon and $CO_2$ from a 80:20 to a 70:30 ratio.

This thesis will first present the AMS-02 detector as a whole and discuss the physics theory and goals in Chapter 2. Chapter 3 concentrates on the physics of the TRD and the optimal design of the AMS TRD. Chapter 4 details the TRD Gas system with focus on design considerations and extensive testing. The electronics and the slow control design and programming is presented in Chapter 5. Finally, AMS-02 capabilities are discussed and conclusions are drawn.

# Chapter 2

# AMS-02

The AMS-02 detector is a large acceptance magnetic spectrometer designed to measure cosmic ray spectra. A precursor flight, AMS-01, flew on board of a Space Shuttle Discovery (STS-91) for ten days in June 1998 at an altitude of 320-390 km, [3, 6, 7, 8]. AMS-01 was a simplified version of AMS-02 with a 0.14 T permanent magnet, and no TRD or Ecal. It collected data on the primary cosmic rays in low earth orbit in the rigidity interval from 0.1 GeV to 200 GeV. AMS-02 will improve on the results of this mission mainly by the introduction of a super-conducting magnet and larger acceptance and exposure time leading to higher statistics and $e^+e^-$ identification.

## 2.1 AMS-02 Detector

The major elements of AMS-02 are shown in Fig. 2-1. The core of AMS is a superconducting magnet. Inside this magnet are 8 planes of silicon strip detectors. Above and below the silicon tracker are two orthogonal planes of time of flight (TOF) scintillator detectors. Complementing the spectrometer is a Transition Radiation Detector, a Ring Imaging Čerenkov (RICH) detector and an Electromagnetic Calorimeter (Ecal). A proposed synchrotron radiation detector [13] addition was later canceled due to the tight weight budget. The detectors are supported mechanically by the USS (Unique Support Structure) which also provides the connection to the Space Shuttle or the International Space Station (ISS). Two star trackers allow AMS to know the

orientation better than $1'$, much better than the ISS instruments. The geometric acceptance is about $0.5m^2sr$ for the full detector. The detector in total weighs 14809 lbs and consumes only 2 kW of power.

The AMS coordinate system is defined by using the wake and ram of the ISS as seen in Fig. 1-1. The vector from the center of the magnet to the wake side is defined as the +Y coordinate axis. The AMS magnet bends particles in the Y-plane. A right-handed coordinate system is used so the port side is in the +X direction in this coordinate system.

AMS measures the rigidity of a particle, its charge and the sign of the charge independently. Finding the rigidity, R, of a particle which is defined as $p/Z$, is also equivalent to making a measurement of $Br$, where $r$ is the radius of curvature. The rigidity is measured mainly from the tracker. The energy deposition in the silicon tracker, the TOF, the Ecal and the TRD also provides independent measurements of the charge of the particle as well as the measurement in the RICH. The sign of the charge is determined from the bending by the magnetic field by the tracking system. The velocity is measured by the TOF, the TRD and the RICH sub-detectors. The multiple measurement of the same physical quantity using different techniques allows for cross-checks. The reconstruction of an event is done using a track fitting algorithm using position and momentum information from all sub-detectors. Here we briefly discuss the magnet and each sub-detector.

### 2.1.1 AMS-02 Magnet

The magnetic dipole field is achieved by an arrangement of 14 super-conducting coils. The two large "dipole" coils will provide most of the transverse field while the smaller 12 "racetrack" coils contain the return flux, as seen in Fig. 2-2. This arrangement minimizes the stray field outside of the magnet, which would be hazardous to the system that provides air to the astronauts during EVAs (extra-vehicular activities) also known as space-walks. The total dipole moment has been minimized in the design because a non-zero dipole moment would exert a torque on the ISS, towards aligning itself with the earth's magnetic field. The coils are all electrically connected

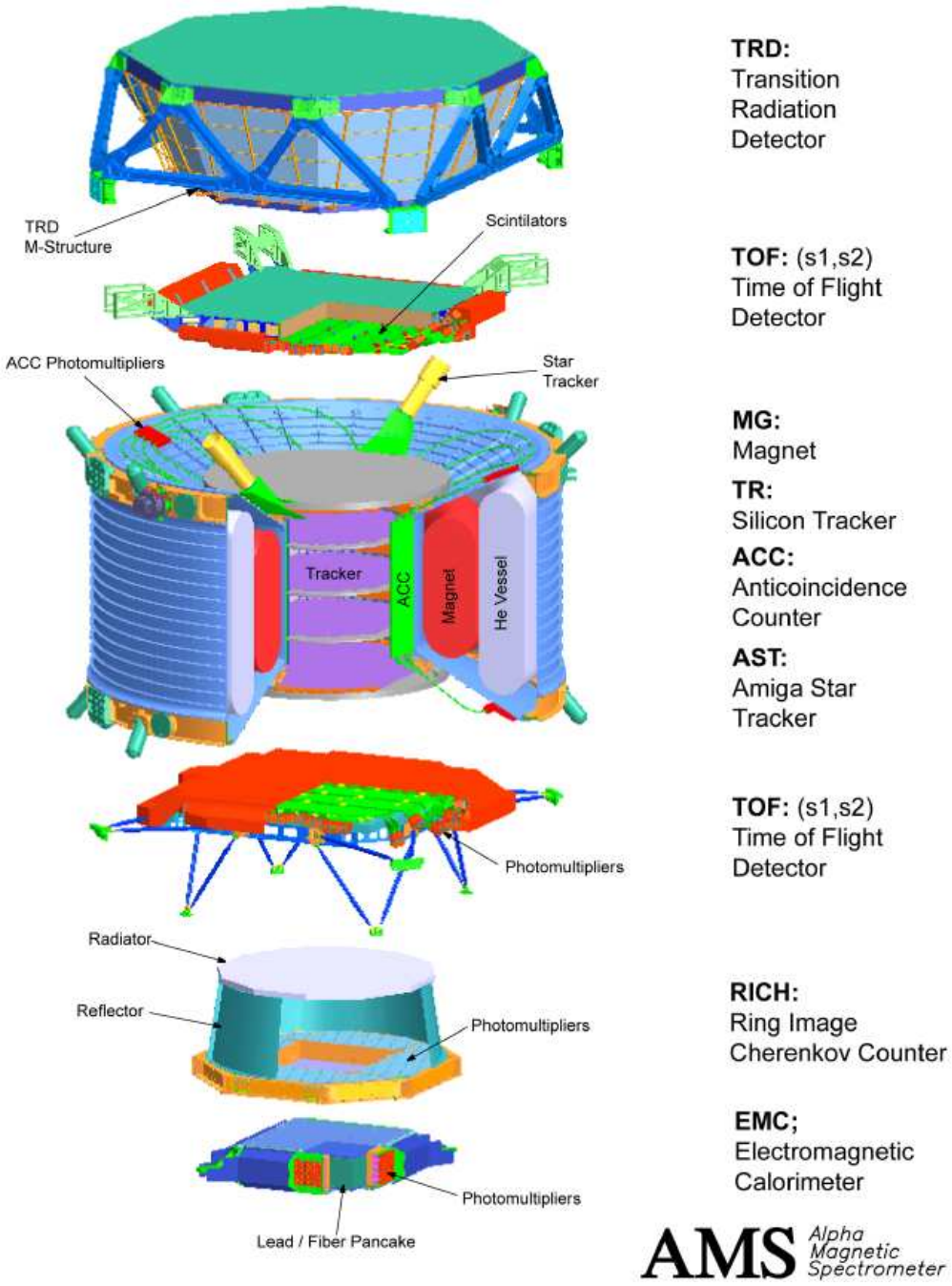


Figure 2-1: An exploded view of the AMS detector.

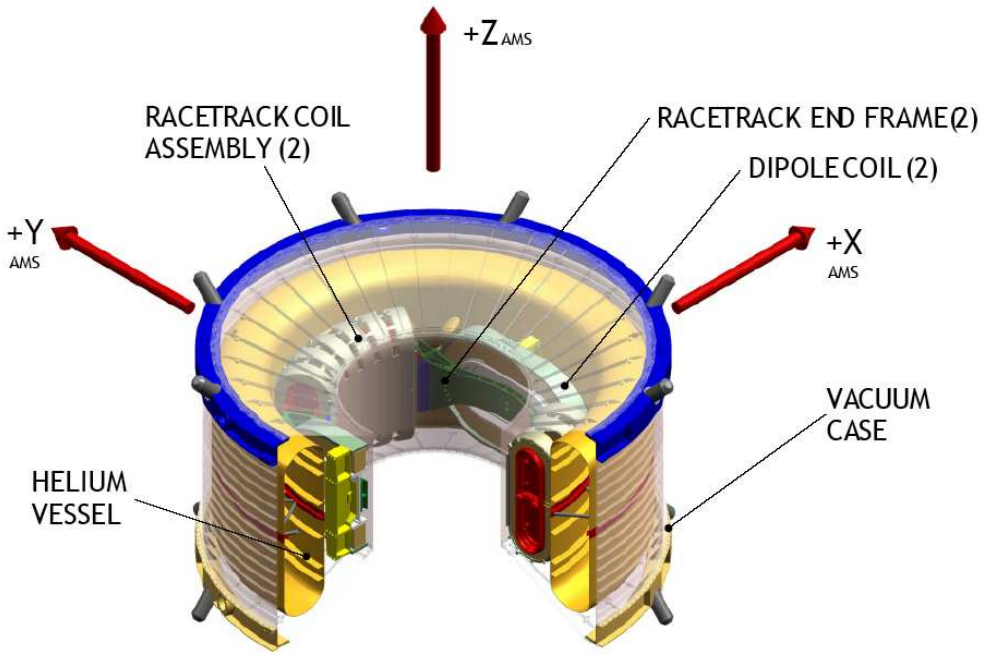


Figure 2-2: The AMS magnet, [36].

carrying a current of 459 A and the total inductance is 48.9 H. The total stored energy is 5.15 MJ. The whole magnet will be cooled to a temperature of 1.8 K by 2500 liters of pressurized super-fluid helium. The system is being constructed by Space Cryomagnetics Ltd in England, [115]. The magnet will be cylindrical in shape with an inner diameter 1.2 m and length 0.8 m. It will provide the 0.86 T at the center of AMS and 0.78 $Tm^2$ Bending power, [74, 36]. The magnet bends particles in the Y-plane of the AMS-coordinates.

### 2.1.2 TRD

The TRD consists of 20 layers of radiator and proportional tube detectors, stacked in a conically shaped octagon support structure. Fleece material of type LRP-375 is used as the radiator, [113]. Xe:$CO_2$ = 80 : 20 filled proportional straw-wall tubes are used to detect the ionization loss plus the TR photons. These 6mm tubes are arranged into modules of 16. There are 328 modules in total with lengths up to 2m. The upper and lower four layers run parallel to the magnetic field whereas the middle

12 are orthogonal to the field. This provides tracking information for all charged particles. The AMS TRD can cleanly separate positrons from the background protons with $10^{-2}$-$10^{-3}$ accuracy in the energy regime between 10-300 GeV. The detector is being constructed by RWTH Aachen and the gas system at MIT. The electronics readout and control is designed by TH Karlsruhe and INFN Roma. A more detailed description is given in Chapter 3.

### 2.1.3 Time of Flight(TOF) system

The time of flight system consists of four layers of plastic scintillator paddles. The scintillation light is collected by two light guides on each side and the two photo-multiplier signals are added together. The light guides have been designed to accommodate for the high magnetic fields present at the photo-multiplier locations. There are two orthogonal layers of counters above the silicon tracker, consisting of eight counters each. Also, below the tracker, there are two orthogonal layers consisting of ten and eight counters respectively. The TOF system provides the trigger for the AMS detector and measures the transit time of singly charged particles with 140psec accuracy, [35, 52]. It also gives information about the energy loss, which is related to the charge of a particle, and coordinates of the particle. The main trigger of AMS-02 is provided by the TOF system. Another set of scintillation counters called anti-coincidence counter (ACC) surrounds the full perimeter of the silicon tracker. The ACC avoids triggering on particles which traverse the detector sideway and complicate the reconstruction of real events.

### 2.1.4 Silicon Tracker

The silicon tracker is composed of $41.360 \times 72.045 \times 0.300 mm^3$ double-sided silicon microstrip sensors, [45]. The silicon sensors are then grouped together, for readout and biasing, in ladders of different lengths to match the cylindrical geometry of the AMS magnet. There are 8 silicon planes and the distance between planes 1 and 8 is one meter. The total area of this double sided silicon detector will be $7\text{m}^2$. The space

resolution in the bending y-plane is 10$\mu$m. The ladders have to be aligned accurately to maintain this high space resolution. The silicon tracker provides the tracking and bending information of the particle essential for the rigidity reconstruction as well as energy loss information, for a charge measurement. This configuration with high precision position measurements provides a great advantage over the different gaseous tracking methods used in several balloon flights. Although the number of measurements is small, the high modularity, low voltage levels (<100V) and gas-free system is a great advantage for space operations. The AMS-01 tracker although smaller, proved this concept and the tracker alignment scheme. The AMS-02 tracker will provide a momentum resolution of 2% at 1 GeV and of 4% at 100 GeV.

### 2.1.5 Electromagnetic Calorimeter (ECAL)

The Electromagnetic calorimeter is a three-dimensional fine-granularity sampling calorimeter with a total of 17 radiation lengths. It consists of 1mm diameter scintillating fibers glued by epoxy between grooves of lead plates. Each super-layer contains 10 layers of scintillator and is 18.5mm thick. The full detector is 9 super-layers alternatively oriented along the X and Y axis with 5 super-layers viewing the bending plane (Y view). Imaging of the shower development in 3D allows for the discrimination between hadronic and electromagnetic cascades. The Ecal will compliment the TRD in the rejection of protons from the positron sample and will provide $10^{-3}$ rejection, [91]. With the final design, the energy resolution of the Ecal is $12\%/\sqrt{E} + 2\%$, [47]. The Ecal can also be operated in single trigger mode and can make measurements of cosmic gamma rays.

### 2.1.6 Ring Imaging Čerenkov Detector (RICH)

The AMS RICH detector has a low refractive index radiator, Silica aerogel with an index of $n = 1.03$, [119]. The Čerenkov photons are collected by a pixelized photo-multiplier matrix with pixel size, 8.5 mm$^2$, [19]. Between the radiator on the top and the photo-multipliers on the bottom, is an empty space of 45.8cm surrounded by a con-

ical shaped mirror, increasing the reconstruction efficiency. [42] Since the Čerenkov angle, $\theta_c = 1/n\beta$, the $\beta$ measurement follows straightforwardly from the Čerenkov angle reconstruction. The velocity measurement from RICH is a very different technique from the detectors that provide velocity information and hence complements them. For singly charged particles, it will provide a $\Delta\beta/\beta$ resolution 0.1% and also help extend the electric charge separation up to iron.

## 2.2 AMS Physics Goals

The high precision detectors described above will enable AMS to exceed the sensitivities reached by previous experiments. AMS will measure charged cosmic rays spectra of individuals elements up to Z $\approx$ 26 into the TeV region and high energy gamma rays up to hundreds of GeV, [26]. AMS will accumulate high statistics and improve on the results of other experiments. It will directly search for antimatter in space, anti-He and anti-C and indirectly search for dark matter, in the gamma-ray, positron and anti-proton spectra, [111, 22, 9]. In addition, the search will achieve high statistics study of light nuclei and isotopes, such as deuterium, tritium, $^3$He and $^4$He. Unstable isotope ions with long lifetime like $^{10}$Be and $^{26}$Al are of particular interest because they provide a measurement of the confinement time of charged particles in galaxies, [40]. The cosmic ray fluxes of these cosmic ray components have never been measured before in such a large momentum range.

Unlike gamma rays which directly point back to their sources, charged particle propagation is complicated by magnetic fields and synchrotron losses. Before we discuss the physics goals, we must pay attention to the propagation of cosmic rays.

### 2.2.1 Cosmic rays

Several elementary particles were first discovered in cosmic rays. Starting with the discovery of $e^+$ in 1933 and continuing with $\mu^\pm, \pi^\pm, K^\pm$ to count a few, [27]. And still, there is much interest in cosmic rays physics due to relatively-new subjects like supernova neutrinos and ultra-high energy cosmic rays. Cosmic rays act as messengers

from the universe and are still largely open to exploration.

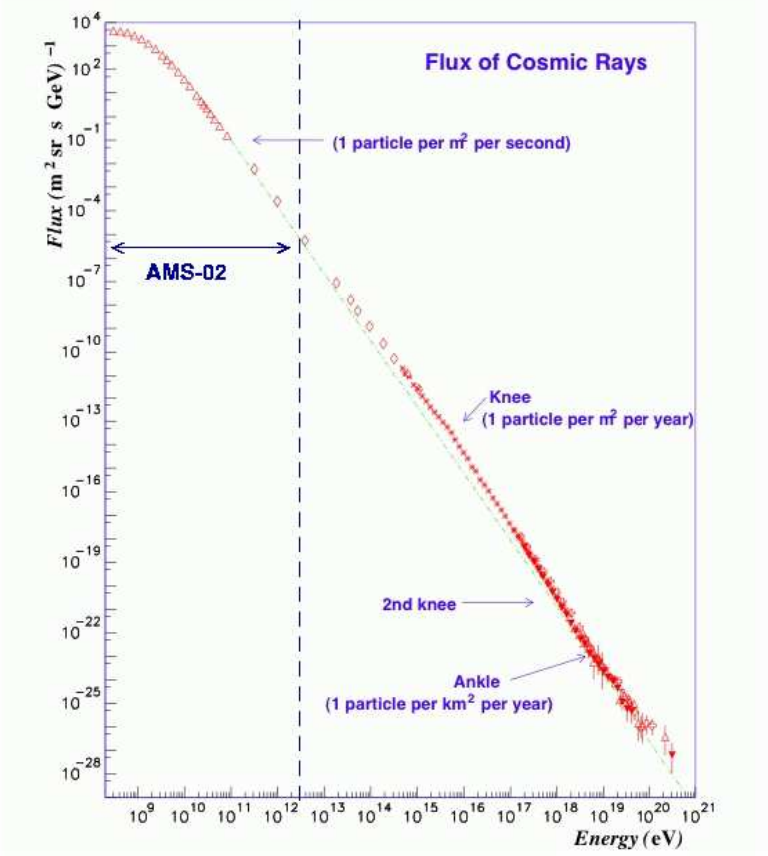


Figure 2-3: The cosmic ray spectrum, [120] and the AMS-02 reach.

The cosmic ray spectrum, as shown in Fig. 2-3, has been measured over a wide momentum range, extending 15 orders of magnitude in energy. Although the cosmic spectrum generally follows a power-law spectrum, there are unexplained features such as the knee, and the ankle where the power law suddenly changes. Also, the Greisen-Zatsepin-Kuz'min (GZK) cutoff region above $5 \times 10^{19}$ eV is being explored, [15]. The spectrum below 10 GeV deviates from the power law behavior and is dominated by the solar modulation. It also depends on the earth's magnetic environment at the observation location, [38]. AMS-01 has measured the primary proton flux in the range 10 to 200 GeV to be $17.1 \pm 0.15(fit) \pm 1.3(sys) \pm 1.5(\gamma)$ GeV$^{2.78}$/(m$^2$ sec sr MeV), [6]. AMS-02 will improve and expand this cosmic proton measurement to 3 TeV.

| Particle | Abundance |
|---|---|
| Protons | 1.0 |
| Helium and heavier elements | 0.15 |
| Electrons | 0.02 |
| Positrons | 0.002 |
| Anti-protons | $1 * 10^{-4}$ |

Table 2.1: Approximate abundances of cosmic rays in the GeV region, normalized to the proton flux.

The general power-law behavior of the cosmic ray spectrum is inherent to the astrophysical mechanism of acceleration, namely Fermi acceleration. When a shock propagates through a plasma, the particles in the plasma get trapped in the shock boundary, crossing it several times and gaining energy repeatedly. The process continues until the particle escapes. The Fermi acceleration, although a simple model, predicts a power law with a spectral index of -2.6, which is very close to what we observe on earth, a spectral index of -2.7. With magneto-hydrodynamic refinements, the observed index can be explained. Also, the synchrotron losses during the acceleration steepen the spectrum.

The cosmic rays that we observe are believed to originate overwhelmingly from inside our own galaxy, from supernovas and from jets or from spallation. Cosmic rays are generally categorized as primary and secondary; primary, if the cosmic ray comes directly from its source and secondary, if produced subsequent to nuclear interactions in the intergalactic medium. Although the extra-galactic component is considered to be small, an anti-nucleus reaching us would have significant meaning. However, charged particles suffer losses as they propagate from their origin to us. Magnetic fields determine the cyclotron radius and hence the trajectories of the particles while they propagate. Using Faraday rotation, it is possible to measure approximately the magnitude and direction of these fields, but there are irreducible uncertainties in this measurement, [73, 29]. Intergalactic magnetic fields are on the order of a micro-Gauss. This means that a $10^6$ GeV proton will have a cyclotron radius of 1 parsec, if we assume that the fields are uniform. By the same token, any scale larger than 1000 AUs will be washed out, if a cosmic ray "photo" of the galaxy was taken

using the highest momentum particle AMS can detect, a 1 TeV particle. A galaxy will trap particles of lower than $10^6$ GeV energies in the magnetic fields. This means lower energy cosmic rays from the center of the galaxy has a harder time reaching earth since their cyclotron radius is too small. Particles with a cyclotron radius comparable to astrophysical scales can escape outside the galaxy. The confinement times for low energy particles to escape from a galaxy can be very long. Using models which take into account the propagation effects allow for particles to enter our galaxy with energies less than $10^6$ GeV/nucleon. They can originate from galaxies as far as 100Mpc away, [2].

Cosmic rays primarily lose energy through ionization of the interstellar medium, bremsstrahlung, Compton scattering and synchrotron radiation. The losses that a particle suffers while propagating is different for hadrons and leptons since electrons and positrons do not participate in spallation, but their radiation losses are higher. The approximate abundances of cosmic rays is given in Table 2.1 in the energy regime that is relevant to AMS but the ratios change slightly with energy.

### 2.2.2 Direct Search for Antimatter

The baryon number density of the universe is inferred from the measurement of the ratio of the present-day number density of baryons, $\nu_B$ to the present-day number density of the photons. The two methods which measure this ratio independently agree on $10^{-10}$. One of these methods uses the primordial ratios of light nuclei calculated by big-bang nucleosynthesis, [46, 101] and the other uses the anisotropies of the cosmic microwave background, [103].

Several baryogenesis theories have tried to explain this number as well as the observed lack of antimatter in our local vicinity in the universe. In models, where there is equal amounts of matter and antimatter present at the beginning of the universe and use an annihilation scenario, get the baryon to photon ratio to be $10^{-20}$, off by 10 orders of magnitude. Hence, theories which seek to explain this ratio must have a physical mechanism which can create a matter-antimatter asymmetric universe from the initial abundances of matter and antimatter at the big-bang. The conditions

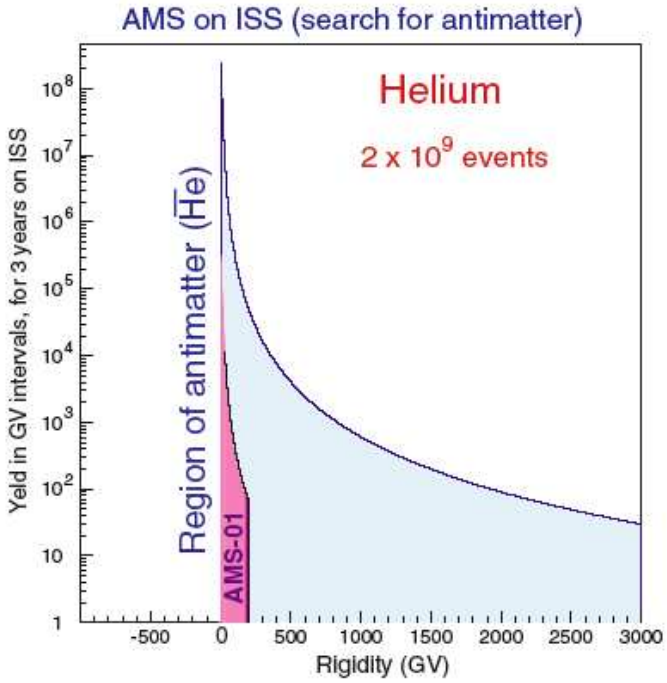


Figure 2-4: Monte Carlo simulation of the AMS-02 sensitivity to anti-Helium, shown with the measurement from AMS-01, [65].

which were laid out by Sakhorov, [106] are: baryon number (B) violation, CP violation and departure from thermal equilibrium. Although CP violation has been observed, the B violation signature, proton decay, has never been observed. There are several theories which try to explain the observed matter antimatter symmetry by trying to satisfy these conditions at some cosmological epoch, such as electroweak baryogenesis, leptogenesis, GUT-scale baryogenesis and Planck-scale baryogenesis, to count a few, [84]. However there is yet no experimental data to support any of these baryogenesis models. Also, no antimatter nuclei has been observed to date.

Distant local distribution of antimatter domains are permitted in some scenarios. Antimatter nuclei from these regions could diffuse through space and eventually reach Earth. The secondary anti-helium in cosmic rays is totally negligible and a detection of just one anti-helium nucleus would be a convincing proof of the existence of these domains. These domains are known to be far away due gamma-ray flux constraints from matter antimatter annihilations. As mentioned earlier, high energy cosmic rays, of the order of 1 TeV, can propagate to our location easier than the lower energy ones.

A detector looking for antimatter increases its chances of detecting an antimatter nucleus if it has this high reach in momentum. Also, an antimatter particle curves in the opposite direction that its opposite sign partner would. Since the determination of sign of the charge is only available through this measurement of curvature, a particle detector seeking to search antimatter must have a magnet, as well as the means of determining the absolute value of the charge.

In the AMS experiment, there are several cross-checks between detectors for the absolute value of the particle's charge and the sign is determined solely by tracking the particle's bending in the magnetic field. Large angle multiple scattering could confuse the reconstruction of an anti-helium event and AMS-02 has been built on a low material budget along the particle's trajectory to minimize this probability. The large, 0.78T, field of the AMS-02 magnet and the $10\mu m$ resolution of the silicon tracker will allow AMS-02 to correctly identify the sign and the charge of an anti-helium nucleus up to 3 TeV.

The best limit on antimatter flux to date has been published by the AMS-01 collaboration. No anti-helium nucleus was recorded in the total sample of 100 million charged particles in the full rigidity range between 1 and 140 GeV, [5]. This translates into an upper limit on the fraction of anti-He nuclei to He nuclei of $1.1 \times 10^{-6}$ at 95% confidence level. AMS-02 is designed to improve this sensitivity by three orders of magnitude as seen in Fig. 2-4. The region studied by AMS-01 is also shown.

### 2.2.3 Indirect Search for Supersymmetric Dark Matter

Our knowledge about cosmology has increased significantly in the last couple of years with the advents of experiments that explore the cosmic microwave background (WMAP), type Ia supernovae (High-Z, Supernova Cosmology Project), large scale structure of the universe (SDSS), quasar absorption studies (Keck, Magellan) and gravitational lensing. The experimental results for the cosmological parameters from these very different methods are consistent. They support the inflationary big-bang theory and have shown that we live in a universe where the total mass-energy is $\Omega_{tot} = 1.02 \pm 0.02$. If the flat universe model is correct, then the best-fit to the data

requires that the universe is composed of 4.4% baryons, 22% dark matter and 73% dark energy, [116, 33].

The nature of dark matter is yet unknown. The baryonic density of the universe is bounded by standard big bang nucleosynthesis and can not explain the total amount of matter density. The neutrino contribution to the matter density is also bounded by the neutrino mass limit and large scale structure studies, [39]. Under these constraints, dark matter must be a more exotic form of matter and the weakly interacting massive particles (WIMPs) are one of the most promising cold dark matter candidates.

There are several WIMP candidates and suggested detection methods, [99]. Perhaps due to the long expectation of particle physicists to find supersymmetry, the SUSY dark matter candidate, neutralino, is the one most invoked. The neutralino, denoted as $\chi$, is defined as the lowest-mass linear combination of the supersymmetric partners of four particles: the photino, zino and the two higgsino states. It is the lightest supersymmetric particle and it is stable if R-parity is conserved. The neutralino mass is thought to be on the order of a few hundred GeVs. The lower limit on the mass of the neutralino from the L3 searches at LEP is 32.5 GeV, [1]. Neutralinos interact weakly and are their own anti-particles. For example, annihilation in normal particles

$$\chi\chi \rightarrow W^+W^-, Z^0Z^0, Z^0h^0, W^+H^-, t\bar{t} \tag{2.1}$$

then offer possible decay paths if the interaction is energetically favorable, [80]. These particles will eventually decay into the few stable standard model particles, such as $p, \bar{p}, \gamma, \nu, e^{\pm}$, through for example $W^+ \rightarrow e^+\bar{\nu_e}$. It might be possible to detect these annihilation products from the galactic halo.

AMS-02 will search for a continuum or monochromatic signal in gamma rays [51], anti-protons, [76] or positrons [91, 87] coming from the Milky Way halo. Looking for a signal in the electron spectrum is also possible, although the background is higher and more difficult to understand. The signal observed in each case is very much dependent on the mass and nature of the neutralino and different scenarios have been

studied, [57, 63]. The possible positron signal is of interest since this is where the TRD will contribute. Neutralinos do not directly annihilate into $e^+e^-$ pairs due to helicity suppression. But if the neutralino is heavy enough and the higgsino content is high, then it can directly decay into monochromatic $W^+W^-$ pairs and the positron from the $W^+$ decay would have a spectrum that peaks roughly half of the neutralino mass. In addition, there would be a continuum of lower energy positrons produced by other decay channels.

Here we only discuss the possibility of supersymmetric dark matter. However, due to a possible strong signal in the positron channel, another model, the Kaluza-Klein model, can be of interest. A first Kaluza-Klein mode of a gauge boson, $B^1$, is a bosonic dark matter candidate. Unlike neutralinos, the $B^1$s can annihilate into $e^+e^-$ pairs which is not helicity suppressed in this model. This decay channel can happen about 20% of the time, and it produces a positron peak at the $B^1$ mass as well as a spectrum of lower energy positrons from other decay channels, [54].

Dark matter content in the universe exceeds the baryonic density by an order of magnitude. It is thought that the visible baryonic matter falls into the gravitational potential created by the clumping of dark matter. According to the present-day understanding, unlike baryonic matter, dark matter can be considered collision-less with baryonic matter. At an early stage in the big-bang, dark matter decouples from baryonic matter and only interacts gravitationally. The baryon-dark matter cross section is limited to being $\lesssim 5 \times 10^{-3} cm^2 gr^{-1}$, [56]. The cross-section is constrained by the changes it would cause in the bang nucleosynthesis calculations and the gamma ray flux originating from pion-decays that are a result of such an interaction. In a galaxy, like our own, visible baryonic matter forms a disk around a tight center, but dark matter is modeled as a halo, not bound to this galactic disk. The observed rotational velocity curves of galaxies suggest that the mass of galaxies are higher than the inferred mass from the luminosity. From these rotational velocity curves, an hypothetical halo mass density profile can be extracted. Simulations indicate that the halo profiles are approximately isothermal over a large range of radii, but shallower than $r^{-2}$ near the center and steeper than $r^{-2}$ in its outer regions, [100]. In our own

galaxy, estimates of the dark matter density typically give $\rho_{dm} \simeq 0.3 GeV/cm^3$, [72].

There is also work on trying to figure out the dark matter substructure from evolution of the the cosmological spectrum of fluctuations inherent to the early universe, [90]. The simulations show that dark matter forms clumpy sub-structure at large scales, long cuspy strings in three dimensions called "caustics", and that they form early on in the universe [110]. Free streaming length for the dark matter particles sets the scale for the length of these caustics. They are thought to be on the order of the solar system scale, rather small compared to the size of the galaxy, [34].

These over-dense regions could in essence enhance the dark matter signal, [114]. According to SUSY dark matter scenario, the annihilation signal from neutralinos is proportional to $< v\sigma > \rho^2$ where $v$ is the velocity of neutralinos, $\sigma$ is a weak-scale cross-section and $\rho$ is the density of neutralinos. An over-density of dark matter compared to the average dark matter density, $< \sigma^2 > / < \sigma >^2$, is called "boost factor." However, before modeling the dark matter positron signal detected on earth, a good understanding of the background positron spectrum and the propagation effects is needed, [97, 17]. The positron background is thought to be mostly secondaries produced by pair production or hadronic interactions. The power-law index of the electron spectrum above 10 GeV is larger than 3.0 in contrast to the proton index of 2.7. Electrons, due to their low mass, loose significant energy by radiation during their propagation through the galaxy, [61]. Similarly, the positron background is expected to fall like the electron spectrum. Our location in the Milky Way is about 8 kpc away from the center of the galactic halo. Calculations show that positrons can diffuse to earth from about 3 kpc, [64] and there could be dark matter caustics within this radius which could enhance the signal. Only after understanding the production, boost factors, propagation and detection, neutralino dark matter signal can be modeled.

The HEAT collaboration has searched for anti-proton signal [28] and a positron signal, [55, 24] shown in Fig. 2-5. They report an excess of positrons in the $10 - 50$ GeV regime with respect to the modeled background expected flux. The possibility that his excess is due to the annihilation in the galaxy has been explored, [78]. Some

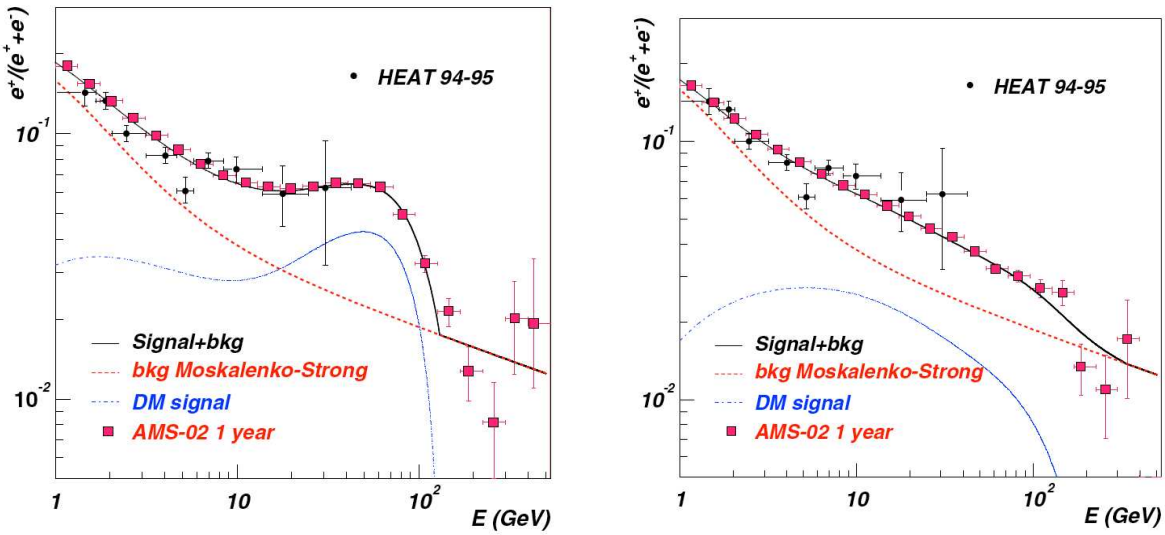


Figure 2-5: The positron fraction in cosmic rays in the case of positrons originating from supersymmetric neutralinos, [17] and superimposed, the expected signal for AMS, [91]. The left side is for the case of a neutralino mass of 335.7 GeV and the right side for 130.3 GeV.

investigations report that the measured excess requires a boost factor that would have to be on the order of 30 or more to provide good fits to the HEAT data, [18]. Such an enhancement could exist if we live in a clumpy halo.

The AMS capability for measuring clean positron spectrum was modeled [111]. AMS will be able to measure the positron spectrum with an energy resolution of 2% and a statistical uncertainty of about 1% at 50 GeV. The possibility of detecting such a SUSY dark matter signal is shown in Fig. 2-5 for one-year AMS exposure for a particular choice of SUSY parameters. Boost factors were chosen to fit the HEAT data. The left hand side is for the case of a neutralino mass of 335.7 GeV and the right hand side for 130.3 GeV, and the positron excess signal is dependent on the mass of the neutralino, [17]. The positron signal from the neutralino annihilations was boosted by 11.7 and 54.6 respectively to fit the HEAT data.[1] The background is described by the positron fraction spectrum from [97]. The separation of positrons from the abundant protons by the TRD is important for such low statistical errors.

[1]The SUSY parameters involved in the calculation of the positron signal can be found in [17] in Table II, examples 1 and 4. The $tan\beta$ parameter is 13.1 for the left hand side and 1.01 for the right in Fig. 2-5.

# Chapter 3

# AMS TRD

Transition radiation detectors have found several application in ground and space based experiments, in providing particle identification. Some recent and new ground based experiments use TRDs for separation of light mesons such as NOMAD [25], MACRO [95, 12], HERA-B [108], D0 [77], E799 [71], ALICE [92] and ATLAS [4]. Balloon and space based experiments, such as WIZARD [21, 32, 20], PAMELA [48, 10], BESS [107] and AMS use TRDs for positron separation from the background protons mainly. There has been some interest in using it for separation of heavier nuclei up to the cosmic-ray "knee," [121] and TRACER experiment has used it to identify some heavy nuclei on a balloon flight, [98].

Several gas supply systems have been designed for experiments on ground, for example, HERMES [118]. However, the AMS TRD gas system is the first one in space that must provide gas for a three year period.

## 3.1 TRD Principle

Transition radiation is the electromagnetic radiation that is emitted when a uniformly moving charged particle traverses the boundary between two media with different dielectric constants, $\epsilon_1$ and $\epsilon_2$. Far away from the boundary, the particle induces fields that are defined by the particle's motion and the characteristics of that medium, such as $\epsilon_1$. Later, when it is the second medium, it has fields that are defined by the

properties of that medium and its motion in that medium. Although the motion is uniform, the fields are different in each media. As the particle is approaching and leaving the interface between these media, the fields have to reorganize to compensate for the change and some part of this compensation is radiated off as the "transition radiation."

### 3.1.1 Generation of Transition Radiation

The transition radiation intensity can be expressed as [60]

$$\frac{dW}{d\omega d\theta} = \frac{2\alpha}{\pi}\theta^3 \left( \frac{1}{\gamma^{-2} + \theta^2 + (\omega_1/\omega)^2} - \frac{1}{\gamma^{-2} + \theta^2 + (\omega_2/\omega)^2} \right)^2 \tag{3.1}$$

where $\gamma$ is the Lorentz factor, $\theta$ is the angle at which the radiation is emitted with respect to the trajectory of the particle, $\alpha$ is the fine structure constant, $\omega$ is the energy of the radiated photon, and $w_1$ and $w_2$ are the plasma frequencies of the initial and final medium, respectively. Using $\epsilon_i = 1 - \frac{\omega_i^2}{\omega^2}$ and integrating over the the angles $\theta$ gives

$$\frac{dW}{d\omega} = \frac{\alpha}{\pi} \left( \frac{\epsilon_2^2 + \epsilon_1^2 + 2\gamma^{-2}}{(\omega_2/\omega)^2 - (\omega_1/\omega)^2} ln \frac{\gamma^{-2} + \epsilon_2^2}{\gamma^{-2} + \epsilon_1^2} - 2 \right). \tag{3.2}$$

Assuming that the initial medium is vacuum, the total energy emitted in transition radiation per interface is approximately [79]

$$I = \frac{z^2\hbar}{3}\alpha\gamma\omega_r \tag{3.3}$$

where $\omega_r$ is the plasma frequency of the radiator and $z$ is the charge of the particle.

There are several features and considerations that need to be highlighted for the optimal design of a TRD.

1. The radiation is proportional to the Lorentz factor, $\gamma$ as seen from Eq. 3.3. Detectors built on this principle are ideal for use in the ultra-relativistic regime where other detectors become ineffective. Detectors with sensitivity to $\beta$, such as the Čerenkov, time of flight, and silicon detectors can not provide a good

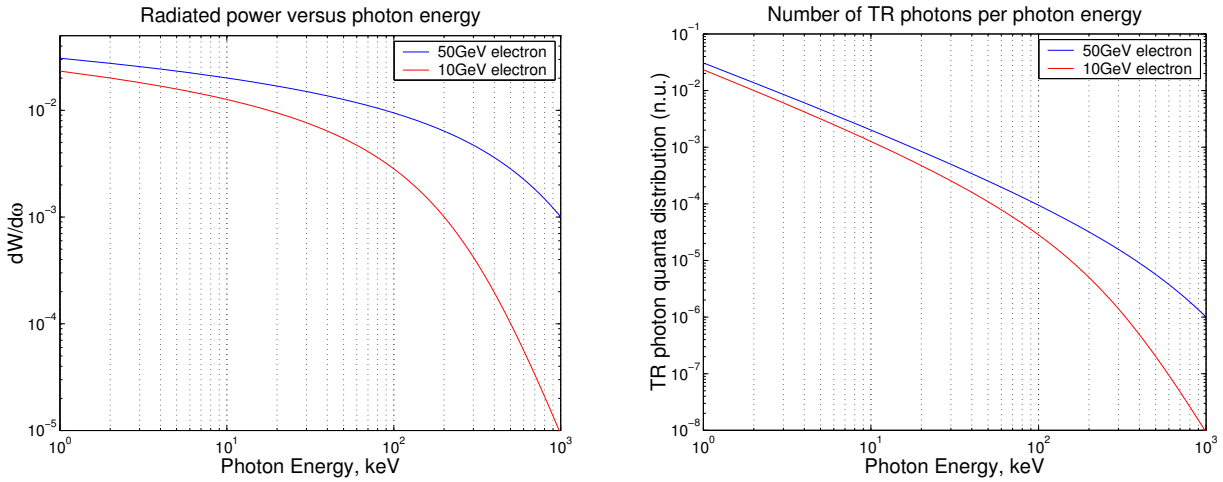


(a) (b)

Figure 3-1: a) Radiated power distribution for photon energies, b) Number of TR photons radiated per photon energy (not normalized). Both, using Eq. 3.1 and 3.2, for transitions from vacuum to polyethylene.

resolution of the energy of the particle in this regime; particle discrimination fails in measurements involving ionization loss.

2. The number of emitted TR photons falls roughly as a power law with the photon energy as seen on Fig. 3-1(b). Depending on the characteristics of the radiator, $\omega_r$, the spectrum of radiation is mostly in the X-ray region. For example, most of the TR quanta for a 50 GeV electron are emitted below 20 keV. However, there is a effective cutoff to the lower end of this spectrum, due to attenuation of low energy X-rays in the TRD materials. This demands that the walls of the proportional counter has to be thin enough to be transparent to most of the X-rays, [59].

3. The probability of creating a TR photon per layer of interface in the radiator is low; on the order of the fine structure constant, $\alpha \approx 1/137$. However, stacking a large number of interfaces of thin radiator material can enhance the TR photon production. On the other hand, there is a balance since increasing the number of material also increases the absorption.

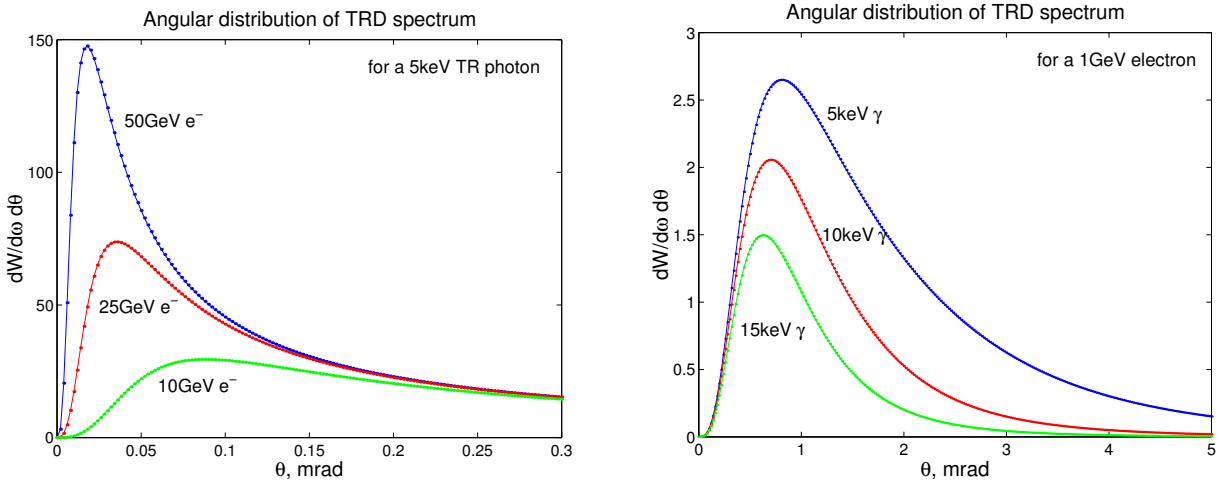


(a) (b)

Figure 3-2: The angular distribution of TR with a) different $\gamma$s and b) different TR photon energies.

4. Most of the TR photon emission is strongly peaked in the forward direction, within the cone of half angle $1/\gamma$, as can be obtained from Eq. 3.1 and can be seen in Fig. 3-2(a). This implies that the ionization energy loss of the particle will be deposited in the detector, as well as the transition radiation component, unless a separation of the particle from the radiation is forced by a magnetic field. In general, such a separation is not necessary if the energy loss of the particle in the medium, $dE/dx$, governed by the Bethe-Bloch formula is well understood and simulated.

These considerations put some constraints on the design of an optimal TRD. First of all, the plasma frequency of radiators, expressed in terms of energy, can vary from 0.7 eV(air) up to 33 eV (aluminum) and this determines how hard the TR spectrum is. The TRD must use a material which is easy to make several layers out of. Also, the generated TR spectrum is very different from the detected one. The gas composition and high voltage of proportional tubes determines the response of the detectors, hence the sensitivity to the TRD spectrum. On the other hand, the absorption of X-rays, between the point they are produced in the radiator to the point in the detector where

they are detected, changes the TRD spectrum. Understanding and quantifying the effects of attenuation due to the materials to balance TR generation and absorption is essential to designing an optimal TRD. This will be discussed further in the next section.

### 3.1.2 Detection of Transition Radiation

The transition radiation X-ray emitted from a radiator cannot be separated in time or space (without magnetic field) from the track of the charged particle that produced the radiation. The TR photon is registered on top of a large ionization background in the detector. Hence, the detector must have the best characteristics for absorption of X-rays and the lowest for the ionization process. The detector has to consist of a thin layer of high Z material, thick enough to absorb of the X-ray, but thin enough to limit the ionization loss, [62]. The ionization signal is composed of initial delta-electrons which in turn create charge clusters proportional to their energy. The energy distribution of these delta-electrons can have a long tail limiting the identification of an emitted TR X-ray.

For the detection of TR radiation, thin proportional tubes can be used with high Z gases. Straw proportional chambers are ideal for detection of the transition radiation since their thin straw walls can minimize the attenuation of the X-rays. Also, the straw in each tube is at ground, avoiding noise pick-up. Any malfunction in one straw will be localized and therefore is isolated from the rest of the detector.

The X-ray radiation ionizes the gas mixture in the drift tube through the photo-electric process, [72]. The number of ion-electron pairs formed will be the energy of the X-ray divided by the mean energy needed to create such pairs. For example, for a 5.9 keV $^{55}$Fe source and $Xe$ gas, which has a pair creation mean energy of 22 eV, the number of ion-electron pairs is 268. These electrons drift towards the wire due to the electric field they feel.

When the electron gets closer to the high-voltage wire and the electric field is large, the electron can pick up enough energy to ionize another gas atom, resulting in two electrons drifting. The primary electron signal is amplified by this avalanching

process towards the high-voltage wire. For avalanche multiplications of $10^2 - 10^4$, the signal pulse is proportional to the initial number of electrons produced. But, the actual signal is formed by the induction due to the movement of ions and electrons as they drift towards the cathode and the signal wire, [88]. Gain is the ratio of the detected number of electrons to the initial number of electrons produced.

It is important to operate drift chambers in the proportional region since the behavior of gain there is well understood: gain is an exponential function of the high voltage on the wire. This must be operated at a proportional region where the signal height is proportional to the signal generated by the particle and the TR quanta, [37]. The AMS TRD is optimized to operate in this proportional regime and with a gain of 3000.

The choice of gas mixture in the straw tube is also important. Efficiency of detecting a TR quanta increases with density. The low mean energy for ion-electron pair creation implies the low field intensities for avalanche formation. Noble gases are best in this aspect. Xenon, being the heaviest and an easy to handle noble gas is the best choice. But, a quencher is needed to avoid UV feedback. UV radiation is produced by transitions within an ionized Xe atom. This radiation can contaminate the signal and to avoid this, quenchers that absorb UV radiation are needed. For the AMS TRD, a 20% gas volume of $CO_2$ quencher will be used.

### 3.1.3 Efficiency of a Transition Radiation Detector

The effectiveness of a TRD system can be quantified by different algorithms. Using the likelihood ratio, or artificial neural networks or support vector machines [11] are common. The efficiency is quantified by a "rejection factor," $\mathcal{R}$, and an efficiency percent, $\mathcal{E}\%$. Say using the likelihood method, we want to choose cuts that will discriminate between protons and positrons. $\mathcal{R}$ is defined as the fraction of misidentified protons in the positron sample. $\mathcal{E}\%$ is the fraction of real positrons that pass the cut. The likelihood, $\mathcal{L}$, for identifying a positron observed with a TRD with $N$ layers,

where the deposited energy is $E_i$ in the $i^{th}$ layer, is defined as

$$\mathcal{L}_e = \sum_{i=1}^{N} log \frac{P(E_i|e)}{P(E_i|p) + P(E_i|e)} \tag{3.4}$$

where $P(E_i|e)$ is the probability that such an energy deposition would be observed from a positron and $P(E_i|p)$ is likewise for protons. The rejection gets better as more and more layers are added. When the cut of $\mathcal{E}\%$ efficiency is defined on the positron likelihood function, it gives us a rejection factor for protons and vice versa. Adding TRD layers, which corresponds to increasing $N$, provides more information about the particle, increases the efficiency of the cut. To achieve the AMS physics goals, a rejection factor of $10^{-2} - 10^{-3}$ at $90 - 95\%$ efficiency is needed for the TRD.

## 3.2 AMS TRD

In designing the TRD, attention has been paid to the balance between generation and absorption of TR photons. A thicker radiator while producing more TR photons, also stops the low energy X-rays, as shown in Fig. 3-3. A 20mm thick layer polypropylene radiator (LRP-375) is used for an optimum generation of TR radiation. The radiator is made out of $10\mu m$ fibers and has a $0.06gr/cm^3$ density. 6mm diameter proportional straw tubes filled with Xe:$CO_2$=80:20 gas mixture are used to optimize the TR photon detection. Also, stiffeners and the support structure is as thin as possible to avoid further absorption. The kapton walls of the TRD are as thin as possible, with 72 $\mu$m but also gas-tight. Measurements of the absorption in the TRD materials and further discussion can be found in [59]. These considerations are important in understanding the energy deposition in each TRD layer.

The proton positron separation increases with adding TRD layers. The AMS TRD has been limited to 20 layers due to weight considerations. Each layer has 20mm of fleece and modules of 16 proportional straw tubes.

The TRD modules shown in Fig. 3-4, are made of a double layer kapton-aluminum foil of 72 $\mu$m wall thickness. Although very thin, they are gas-tight. The gas is

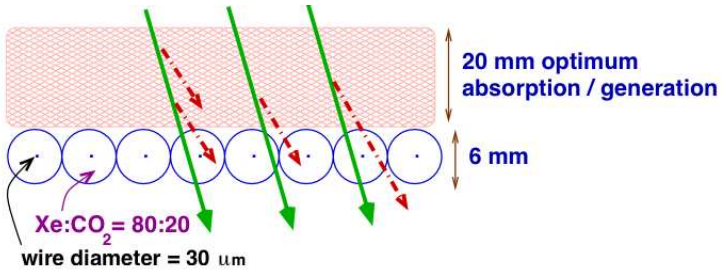


Figure 3-3: The TRD consists of 20 layers of such polypropylene radiator and Xe:$CO_2$ filled tubes for detection.

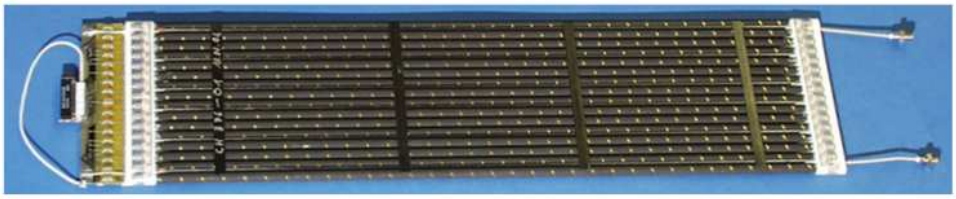

Figure 3-4: 16 straw TRD module produced by RWTH Aachen I, [109].

distributed through them using polycarbonate end-pieces which also center the crimp plugs holding the wire. The Cu-Te crimp plugs hold a 30$\mu$m gold-plated tungsten wire tensioned with 1N. To assure the mechanical rigidity of these modules, there are longitudinal and vertical carbon fiber stiffeners. There are in total 328 modules in the AMS TRD.

The TRD layers are fitted into an octagon made of carbon fiber and aluminum honeycomb seen, in Fig. 3-5, which is machined to 100 $\mu$m precision. Due to this geometry, the TRD modules are all different sizes, longest being 2m. They are supported by two bulkhead in the octagon structure. The upper and lower four layers of the TRD run parallel to the magnetic field where as the middle 12 are orthogonal to that, providing more tracking information in the bending plane.

Gas-tightness is a critical design issue, [113]. The gas supply has to last for three years of operation. Diffusion through the straw foils is different for Xenon and $CO_2$. The estimated diffusion rate for the 230 liter TRD is low enough that only 300 grams of each gas component is lost by diffusion in 1000 days. However, the TRD modules leak sometimes more than this diffusion limit due to gluing of the gas feeds and other

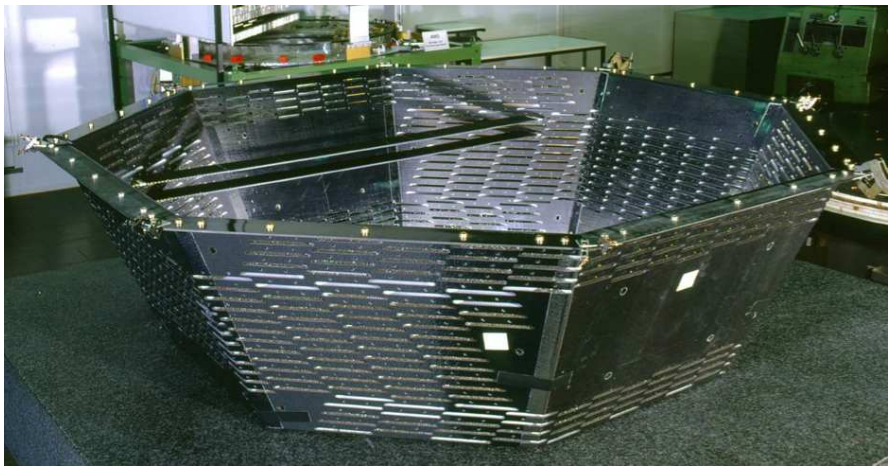

Figure 3-5: The TRD octagon shown with two inserted TRD modules at RWTH Aachen I, [81].

reasons. In space, the TRD might leak more after the vibration it undergoes during launch. To address this issue, several leaks test have been performed, some after a vibration test. The TRD schedule was changed to include production of new straws and test each straw prior to module assembly. Only modules which leak less than $10^{-4} lmbar/s/m$ are accepted as flight modules, [82]. At this rate, the TRD gas supply system has enough gas to last for 12 years of operation.

The AMS TRD proportional tubes will be operated at a gain of 3000 with the Xe:$CO_2$ gas in the tubes at 1.2atm. This pressure will prevent collapse of straws of the TRD before launch at Kennedy Space Center. The high voltage of the proportional tubes is foreseen to be kept at 1500V although this can be adjusted with changing temperature, pressure and gas ratio.

## 3.3 Efficiency of the AMS TRD

The proton positron separation of the AMS TRD has been simulated in detail, using Monte-Carlo code based on Geant 3.21, [53], with additional code to include the TR photon generation and absorption, [62] and to improve the energy loss Landau fluctuations in thin gas layers. The full geometry of the TRD has been used including the support structure and details like stiffeners and bulkheads. The test-beam data was

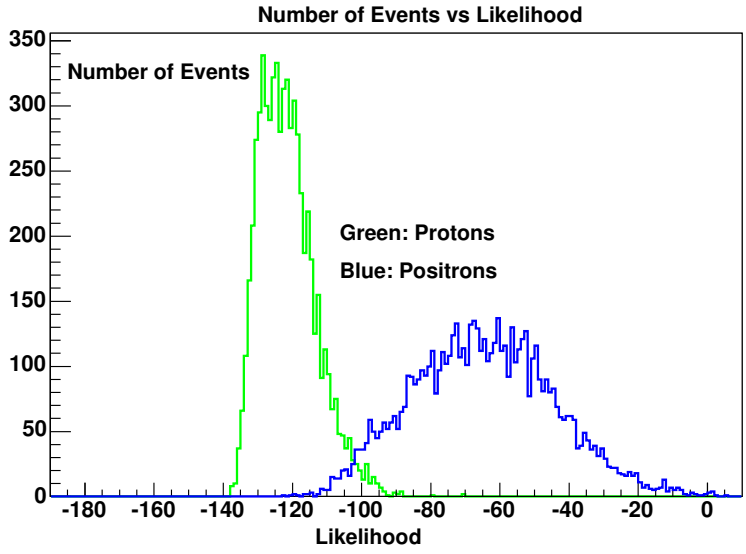


Figure 3-6: Likelihood distributions functions from a Monte Carlo simulation for 50 GeV electrons and positrons, [50].

used to fine-tune the simulation parameters. The separation can be characterized by the likelihood algorithm, using the different energy losses, as in Eq. 3.4. The likelihood function can separate between the simulated proton and positron distributions distinctly, as shown in Fig. 3-6, [50], for the case of mono-energetic 50 GeV particles. Here the horizontal axis, $\mathcal{L}_e$, does not correspond to any physical quantity but is useful for defining a cut. With a cut defined at some specified likelihood value, the particles with higher likelihood value will be identified as positrons. As the cut is chosen towards higher values of this likelihood function, although more and more number of positrons will be misidentified and statistically "lost," the proton contamination goes down. Since the proton flux is much greater than the positron flux in cosmic rays, for AMS, proton contamination has to be as little as possible while maintaining high statistics for the positrons. A 90% positron efficiency point has been chosen as the "working point" since it introduces as little as 0.1% proton contamination. The efficiency of the flight TRD will be determined before flight by a cosmic test and a test beam.

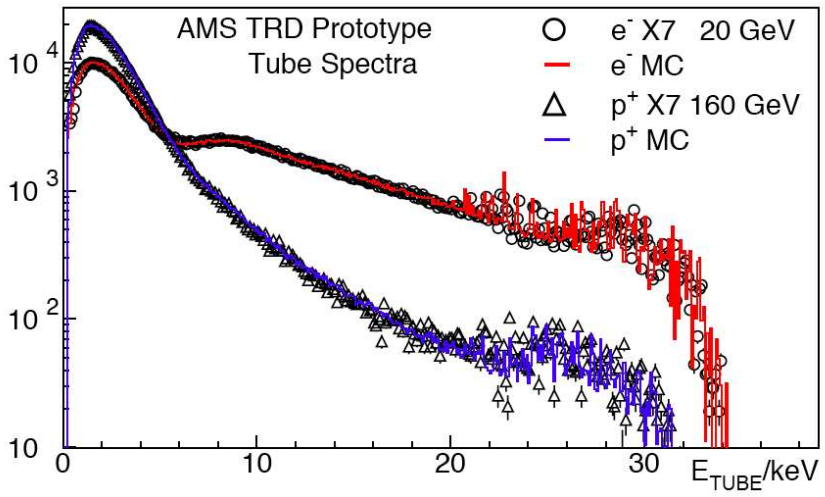


Figure 3-7: The frequency versus energy deposition in one TRD layer using clean single-track test-beam data for 20 GeV positrons and 160 GeV protons, [83].

## 3.4 Test of the AMS TRD

To verify the projected performance of the TRD, a full 20 layer prototype was built with 40 modules of 40 cm in length. The prototype filled with Xe:$CO_2$ = 80 : 20 went under a test beam at CERN in the summer of 2000. 3 million tracks in total of protons, electrons, muons and pions were collected, [83]. An inter-calibration precision below 2% was achievable using 5000 muon tracks. The energy deposited in the TRD is different for 160 GeV protons which only have ionization losses and for 20 GeV positrons which deposit energy from TR photons and ionization losses in the tube. This effect is dramatic above 6.5 keV, as seen in Fig. 3-7.

The electron proton separation obtained from the beam test is better than $10^{-2}$ with 90% positron efficiency. For assessing the test-beam results, a simpler approach than the likelihood method, called "cluster counting", was used. A cluster is defined as a tube with an energy-deposition above some energy, generally in the range $5-8$ keV. Events are selected as positrons if they have more than a certain number of clusters, called "hit-cut". For example, "hit-cut 6" means, that 6 tubes in 20 layers has an energy deposition higher than some pre-defined energy, such as 7.5 keV, then we identify the particle as a positron. Since this analysis does not use the full information,

it is not as efficient as a likelihood method, but it is useful for comparison with other experiments. While the likelihood method uses a continuous distribution of the particle's probability of being an positron, the"hit-cut" method uses a "discrete" distribution of probabilities. In the "hit-cut" method, 10 keV energy deposition in a TRD tube has the same weight in determining the particle's identity as a 30 keV deposition whereas in the "continuous" likelihood distribution, a 30 keV deposition would have more weight.

The distribution of the number-of-clusters can be calculated using binomial statistics if the probability for a hit is taken to be above the energy-cut from the single tube energy distribution. Deviations from this binomial expectation indicates that there is a non-statistical correlation of the clusters due to effects other than transition radiation photons, for example, secondary particles or particle pairs in the beam. To reduce the beam induced effects, strong "single-prong" preselection cuts were applied to the test-beam data to reliably estimate the proton rejection power with clean events. These preselection cuts, which ranged from $40 - 80\%$ of the events, changed for each test-beam run, reflecting the different target and beam collimator settings. With a Monte Carlo simulation, single-prong preselection efficiencies, $P^{sing}$, at the $90 - 95\%$ level was confirmed.

Using a sample of 10 GeV protons and positrons from the test-beam, the proton rejection was calculated for different cuts, as seen in Fig. 3-8. The single-prong preselection cuts and the cluster counting of "hit-cut 6" was used. The energy deposition required in each tube for identifying it as a cluster was varied. Increasing this energy deposition requirement results in higher proton rejection, but lowers the positron efficiency as expected. A change of gain of the TRD can effect the performance of the TRD and this will be discussed in the next chapter using this same plot.

The prototype TRD achieved having as little as 0.1% proton contamination while keeping a 90% positron efficiency with 10 GeV particles. The optimal cut for the flight TRD will be determined from future test-beam data with the flight TRD and will be used in flight with the calibration obtained on earth.

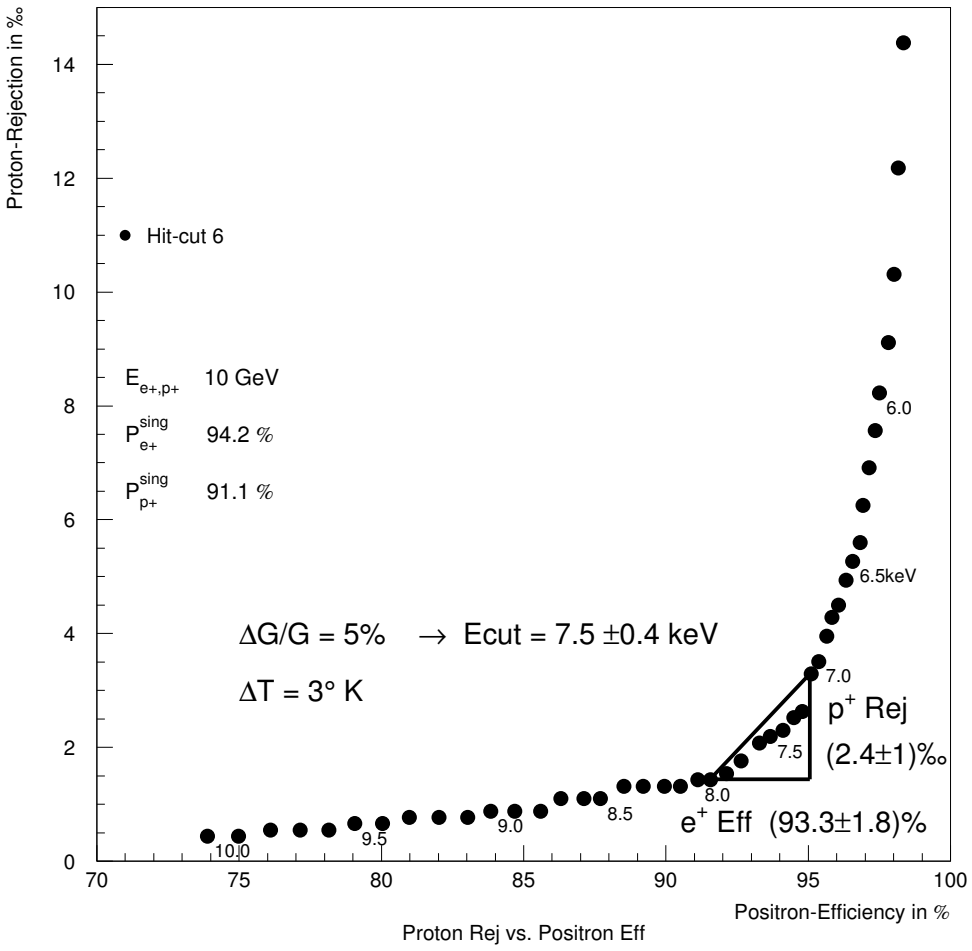


Figure 3-8: Proton rejection versus positron efficiency using test-beam data for 10 GeV particles, [112].

# Chapter 4

# Stability of the AMS TRD and the Gas Supply System

The TRD rejection relies on the signal height of the proportional tubes. The gain is a strong function of the density of the gas and the mixing accuracy. To obtain the required discriminating power of the TRD and to keep the signal height calibrated, a stringent control of the gas parameters are necessary. Therefore, the rejection critically depends on the accuracy of the gas supply system.

## 4.1 Stability of the AMS TRD

The stability of the gain of the TRD is important for the addition of datasets and positron proton separation. Large data sets are needed for establish the optimal cut between positron and proton likelihood functions. A 3% stability of gain has been set as a benchmark goal, needed to achieve the physics goals, using TRD simulations [85]. The effect on the TRD rejection of gain change can also be understood analytically using the "hit-cut" method as we will discuss here.

The TRD gain will change during AMS operation in space due to temperature fluctuations. On orbits with high inclination, the temperature gradient during one day could be as large as 60$^o$C. Also, due to the unavoidable slow leaking of the straw tubes, the pressure will be slightly different in each TRD module. There will be temperature

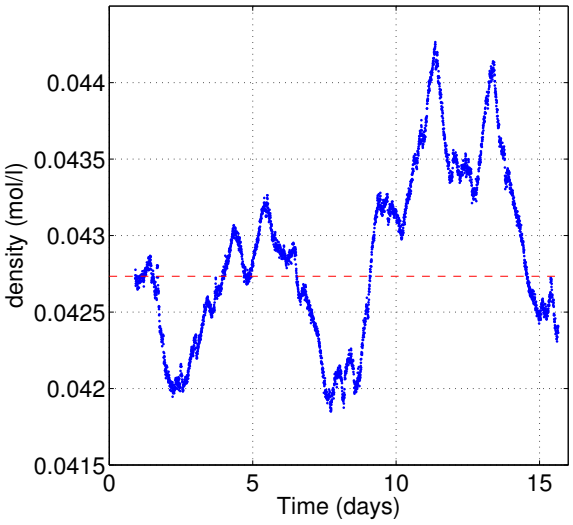


(a) Density fluctuations around reference conditions.

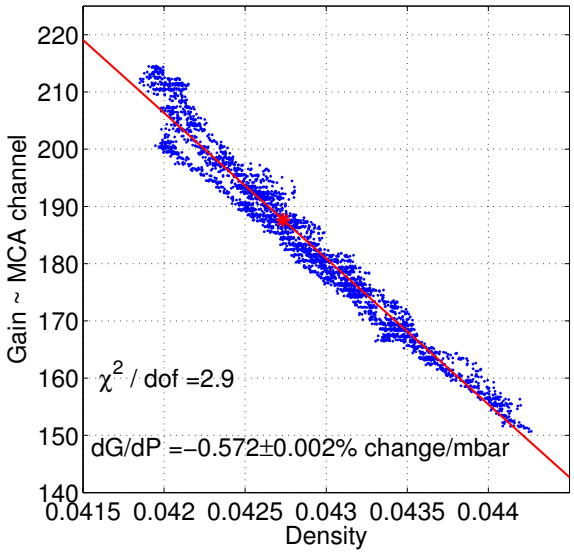


(b) Gain versus density fluctuations are linear for small variations.

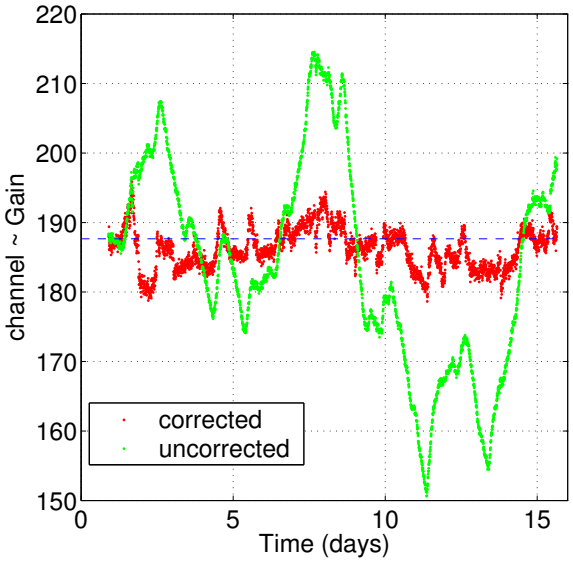


(c) Corrected and uncorrected gain

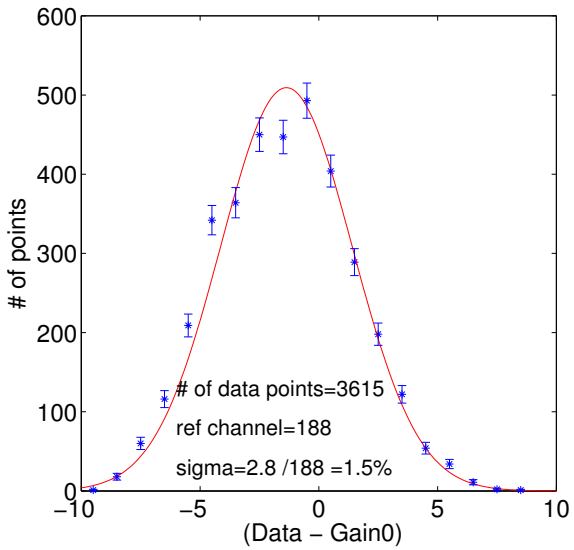


(d) Variations of gain around reference conditions

Figure 4-1: Using premixed Ar:$CO_2$ = 80:20, the density fluctuations were corrected for, at a reference gain of 3000.

sensors embedded in the TRD. Pressure sensors on each end of each segment will be integrated to the TRD as part of the "Manifolds" system. With the knowledge of the temperature and pressure of each segment, the gain can be normalized to a pre-selected condition, such as a pressure of 1.2 atm and a temperature of 21$^o$C. All AMS data sets have to be normalized to these conditions, so that the calibrated cuts, for a clean positron sample, can apply.

The density fluctuations in the gas if well known can be corrected for. The principle of density fluctuation corrections was tested out using a 40 cm TRD module and a $^{55}$Fe source that produces a 5.9 keV X-rays. The temperature, the pressure and the gain was recorded over two weeks as shown in Fig.4-1, using premixed Ar:$CO_2$ = 80 : 20 gas at a gain of 3000, called $Gain0$ here. The pressure sensor, Omega model PX203-0305V, [102] was accurate to 0.25% and the temperature sensor, Omega model DP116-TC2, was accurate to 0.1$^o$C. However, a drift was observed in the pressure sensor during the data taking as well as sudden jumps in the temperature reading which increase the systematics. Without temperature and pressure corrections, the original gain fluctuations are about 6%. The gain can be corrected for the density fluctuations around the chosen gain, $Gain0$, by plotting the gain versus the density. Gain is approximately linear around small perturbations of density and the slope gives a 0.57% change in gain per change in pressure(mbar). As shown, the gain be corrected to $\leq$ 1.5% in this case.

In flight, the temperature and the pressure has to be monitored carefully in the TRD tubes themselves, accurate enough to be able to achieve the 3% gain stability. To establish this stability in gain, there is a need for monitoring the gain of the gas independently and also the $CO_2$ content. Studies show that there is an 8% change in gain per 1% change in the $CO_2$ concentration in this gain regime, [82]. Using the test-beam muon data, the change in gain per one percent change in density of Xe:$CO_2$=80:20 has been measured to be about 5% per 1% change in gain.

The effect of gain change on the rejection of the TRD can be dramatic if it is not limited to the benchmark goal of 3%. Using the "hit-cut" method, a particular energy deposition in a TRD tube is selected and defined as a cluster, [67]. A change

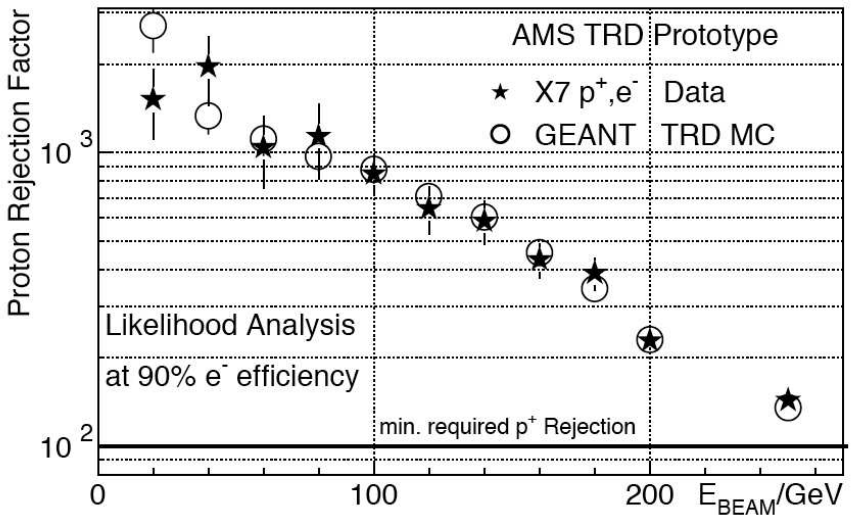


Figure 4-2: Proton rejection versus test beam energy, [83].

in gain changes the gas-amplified signal and effectively moves this cut. For example, a 7.5 keV deposition in the TRD tubes will have an uncertainty of 0.4 keV if there is a gain fluctuation of 1% or $3^0$C as the example in Fig. 3-8. Such an uncertainty in the cluster counting algorithm amounts to an uncertainty in the proton rejection of 1.8% around the 93.3% efficiency point and an uncertainty of .1% around the 2.4% efficiency point. At higher positron efficiency, the effect can be very dramatic. The final TRD cuts will be optimized for 90% positron efficiency, where the slope of proton rejection versus positron efficiency is less, which means, less uncertainty in the TRD performance. However, this plot shows test-beam data for 10 GeV and at higher energies, where the proton rejection is poorer, the TRD performance can be effected more. The proton rejection versus the test beam energy is shown in Fig. 4-2. For this plot, the test-beam electron energy was constant at 20 GeV while the proton energy was varied. Since the electrons are already ultra-relativistic at 20 GeV, the rejection does not change much if the electron energy is increased. This was cross-checked at the test-beam, by using a lower-statistics sample of 100 GeV electrons. The energy deposition in the TRD was the same as for 20 GeV electrons. This gives a handle on understanding the effect of gain change on the performance of the TRD and makes the case for having a good control of the gas parameters.

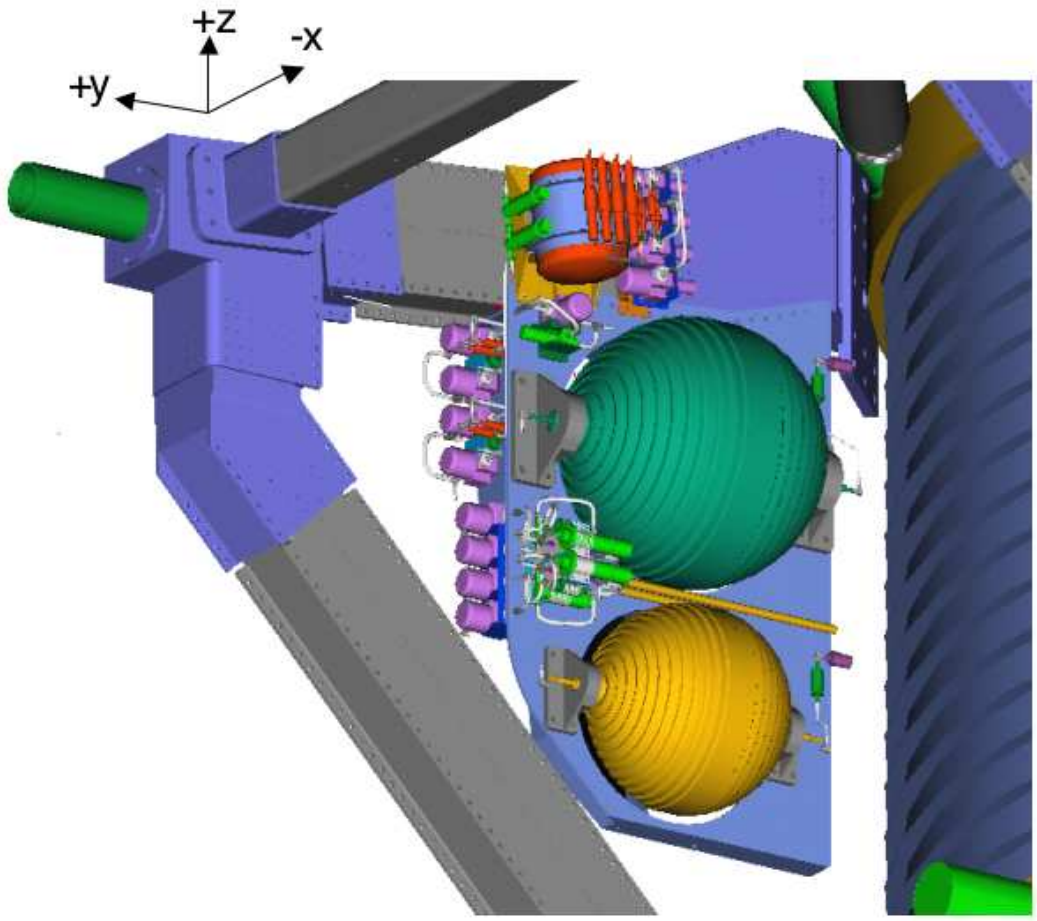


Figure 4-3: Box S and C shown sitting on the AMS support structure with the relative AMS coordinate system. The vacuum case for the magnet is shown on the right.

## 4.2 TRD Gas Supply System

The system comprises of a module for supply (Box-S), one for circulation(Box-C), and gas manifolds for distribution, [31]. These subsystems will each be under the control of redundant and dedicated electronics cards which communicate to the main data acquisition computer through a Universal Slow Control Module(USCM). Box S will mix and provide the 7 liters of gas needed to replenish the TRD every day. Box C transfers the fresh gas to the TRD volume and circulates the full TRD volume three times a day increasing uniformity and monitoring gas parameters. The monifolds distribute the gas to the TRD module, detect leaks and isolates them if needed. The gas system has been designed under a tight weight budget of about 120 kg.

Box S and C are located in the +X and +Y quadrant of AMS as shown in Fig. 4-3. Both boxes are placed in the wake side of ISS since the chances of a meteorite hitting the high pressure gas tanks is much less on the wake side. Also the corresponding "UG" electronics crate is positioned close to the gas system. The manifolds are mounted directly on the TRD octagon support structure.

### 4.2.1 Gas Supply Box

Box S will mix Xenon and $CO_2$ gases to the necessary proportion using the law of partial pressures. A series of high pressure valves and pressure sensors in the supply unit will mix the gas into a buffer volume. About 109 lbs of Xenon and 11 lbs of $CO_2$, are needed for the full mission. Box S carries these supplies of Xenon and $CO_2$ in lightweight carbon fiber over-wrapped stainless steel tanks, produced by Arde, [14]. These leak-before-burst vessels ensure safety. For example, in the event of high temperatures and if the vessels can not be vented through the gas system because of a power-off, the vessels are still safe.

The high pressure gas is controlled by a cascade of solenoid valves and is opened to increasingly larger buffer volumes to reduce the pressure as seen in Fig.4-4. At the last step, the gas is metered through a flow restrictor, O1a or O1b, of a well-known time constant into the mixing tank, Vessel D. By controlling the opening times of the V3a and V3b valves, the gases can be added in partial pressures, using P2a and P2b, to the desired mixing ratio (80:20 in general). The pressure sensors used in the system are accurate to 0.15% and three fold redundant. In the gas system, there are 14 valves in total. 2 valves (Va and Vb) will only be used for filling Box S at Kennedy Space Center and will not be used in flight.

To test the principle of Box S, a prototype was built at MIT, [75]. An engineering version, which is identical to the flight version was completed at CERN in 2003, except the flight tanks, [44]. When AMS is in space, each command will be tested out on this engineering copy on earth before being issued. The flight version will be built by Arde Inc, [14].

To facilitate the integration of Box S, the components are grouped into sub-

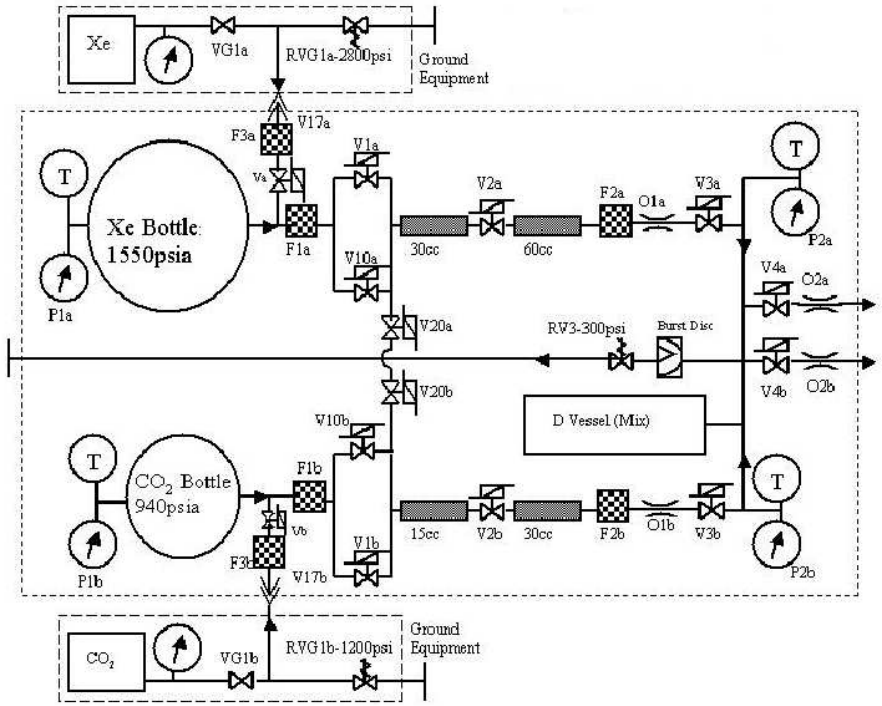


Figure 4-4: The schematic flow of the gas supply box, Box S.

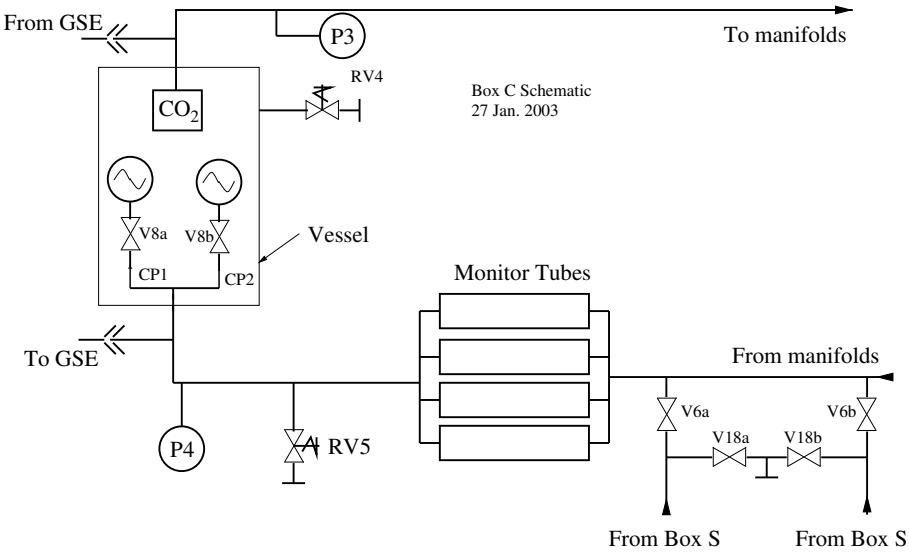


Figure 4-5: The schematic flow of the circulation box, Box C.

assemblies as seen in Fig. 4-6. First, each subassembly is welded together in the designed holders, or brackets. Then joined with other sub-assemblies on the Box S structural plate. The piping that is used is SS316 which is orbitally welded. Mostly 1/8" tubing is used, but the buffer volumes are made from 1/2" tubing.

The design has to be two-fault tolerant and redundant wherever possible. Valves V1a and V1b are redundant. If one mixing branch fails, mixing can proceed through the other branch using V20a and V20b. These valves are used back to back to avoid gas from leaking across if one valve fails open. If one branch fails, opening these two valves at the same time allows gas to be mixed through the other branch. Also, a relief valve is placed on Vessel D behind a burst disk, in case the relief valve leaks.

The engineering Box S underwent extensive space qualification, to assure its survival under harsh vacuum, thermal, and vibration conditions. In Fig. 4-7, it is shown undergoing vibration test in Cassacia, Italy. Mass equivalents were used for the Xenon and $CO_2$ tanks. Box S components, the solenoid valves and the pressure sensors have been tested separately as well. Since their performance is effected by being in the ambient fringe field of the AMS magnet, they have been moved to the side that is less prone to magnetic fields, as shown in 4-10. They have been tested extensively at the maximum field strength of 600G.

### 4.2.2 Gas Circulation Box and the Manifolds

The circulation box (Box-C) was designed to exchange three TRD volumes (230 liters) per day. This increases the uniformity of the gas through the TRD volume. Box C contains two redundant diaphragm pumps driven by brushless motors. A high-pressure valve, V6a or V6b, allows Box C to admit fresh gas from Box S through a flow restrictor. Valves, V18a or V18b, can be used to vent gas into space. To pressure sensors again accurate to 0.15% will determine if there are any fluctuations in gas pressure. One is upstream of the pump and one is downstream, which monitors the pump speed as well.

Box C uses two techniques to monitor the gas quality. There is a 6mm proportional tube which contains $^{55}$Fe sources. Fe produces a spectrum with a 5.9 keV line allowing

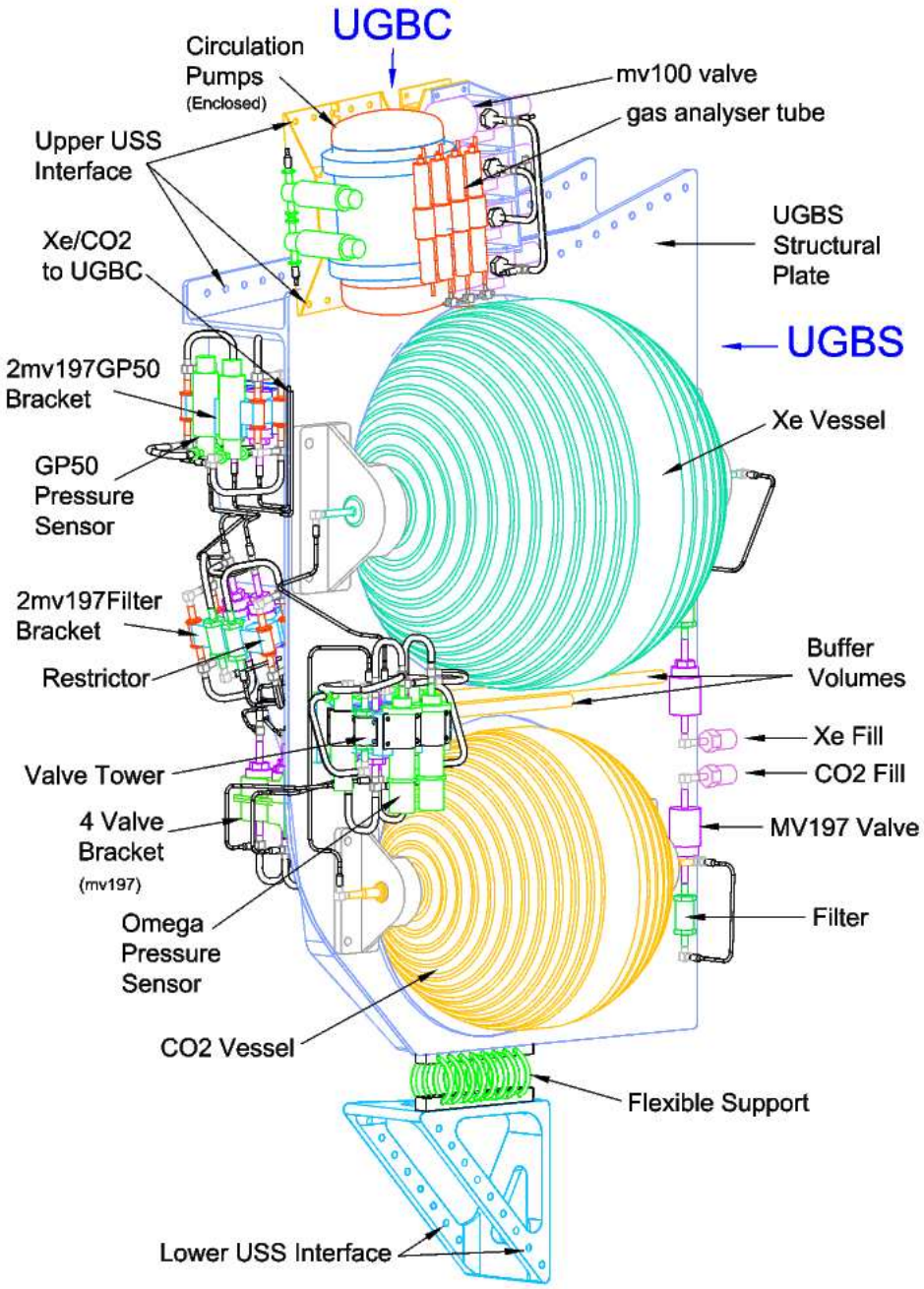


Figure 4-6: The mechanical drawing of Box S and C from [30]. Color coding indicates: green for pressure sensors, purple of solenoid valves and red for flow restrictors and calibration tubes.

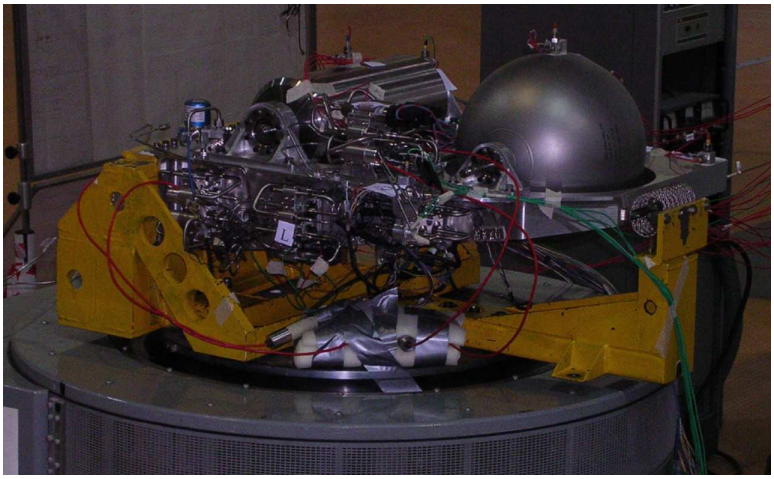

Figure 4-7: The engineering Box S undergoing vibration tests, [66].

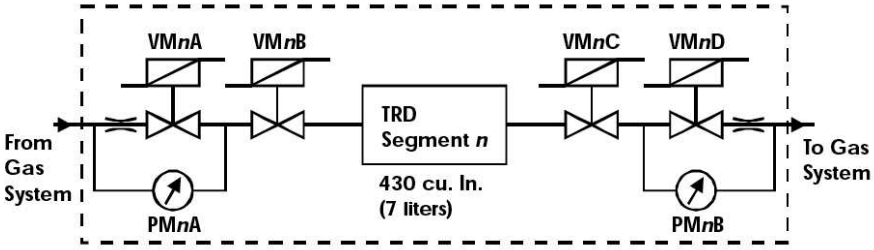


Figure 4-8: The schematic flow of the manifold sub-circuits.

an independent calculation of the gain. A spirometer, commonly used in medical industry, measures the speed of sound in the gas which depends sensitively on the gas mixture. The spirometer measures the transit time of an ultrasonic pulse through 52mm of gas; the transit time increases with decreasing $CO_2$. Corrections to the ideal gas approximation are required in order to measure the mixture to an accuracy of 0.15%, [96]

The pumps and the $CO_2$ sensor will be mounted inside a gas tight vessel so that in the event of a pump or valve leak, the pressure integrity of the system will not be lost.

Manifolds distribute gas throughout the detector using 41 gas sub-circuits. The two differential pressure sensors on each circuit can rapidly detect the increased flow rate associated with a puncture, and any of the gas sub-circuits can be shut off if

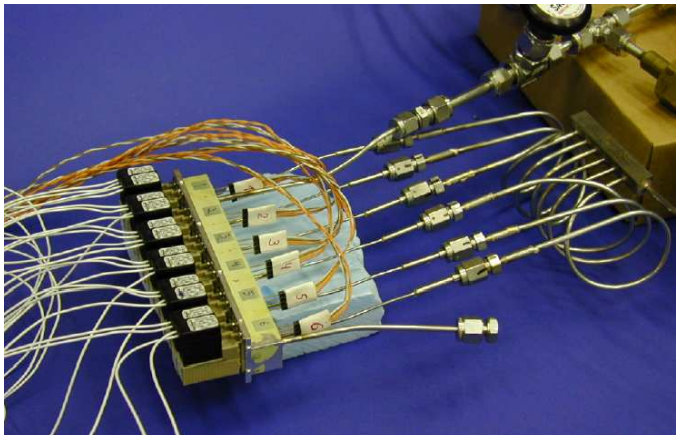

Figure 4-9: Manifolds in functional testing.

this occurs, using bistable "flipper" valves at entrance and exit of submodules. The manifolds also allow diagnostics by periodically looking for localized pressure drops by closing all of the valves. Each manifold sub-circuit will be be housed in mu-metal, a soft ferromagnetic high-Nickel content alloy, to shield the flipper valves from the fringe field of the AMS magnet.

## 4.3 Box S Components and Testing

The testing of Box S components fall under two categories: tests done to satisfy NASA safety requirements and those done to ensure AMS mission success. For example, some NASA safety requirements that are important for the gas system are tracebility of each component, limits on out-gassing of components, a lower limit of 60 Hz vibrational modes on each structural component, and that all high pressure components must be built to hold 2.5 to 4 times more pressure than they will hold while in operation in flight. For AMS mission success, each component has to work in the fringe field of the AMS magnet and has to work reliably for three years, and the design has to be fault tolerant where ever possible. Details about components not mentioned here can be found in [31].

### 4.3.1 Magnetic Field

A stray field map of the AMS magnet has been prepared by Space Cryomagnets, [115]. This field map extends to (150, 150, 65) cm in (x,y,z) coordinates with a granularity of 5 cm in all directions and all quadrants are symmetric. However, Box S extends well beyond this in the y-direction. The field map was extrapolated by the author using power-laws and and re-calculated at a granularity of 1cm. Box S can be considered to be a plane at x = 90cm. The contours of field strength are shown in Fig. 4-10. All sensitive components were moved from the lower-y side with fields of 1000G to the higher-y side of Box S with fields of 400G. While complicating the design and plumbing, it provides a safety margin for the nominal performance of all components. Some components sit above the Box-S plane, for example, at x = 80cm, this increases the field by 150G at the maximum. So all components have been tested at this maximum field of 500G or higher. Also, the magnetic field direction has been calculated at each step as shown in Fig. 4-11 and the valves have been placed orthogonal to the direction of the B field where ever possible.

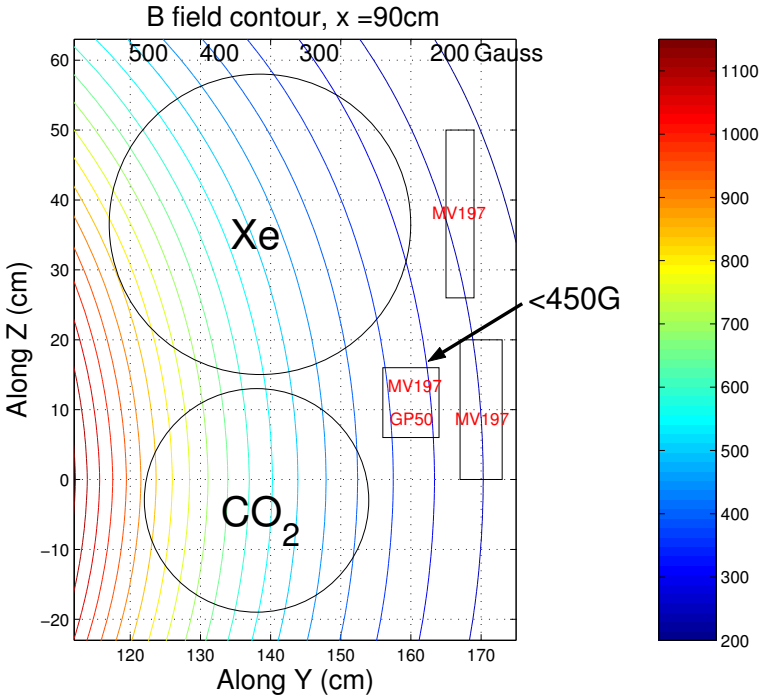


Figure 4-10: The magnetic field strength in the x =90cm plane in AMS coordinates.

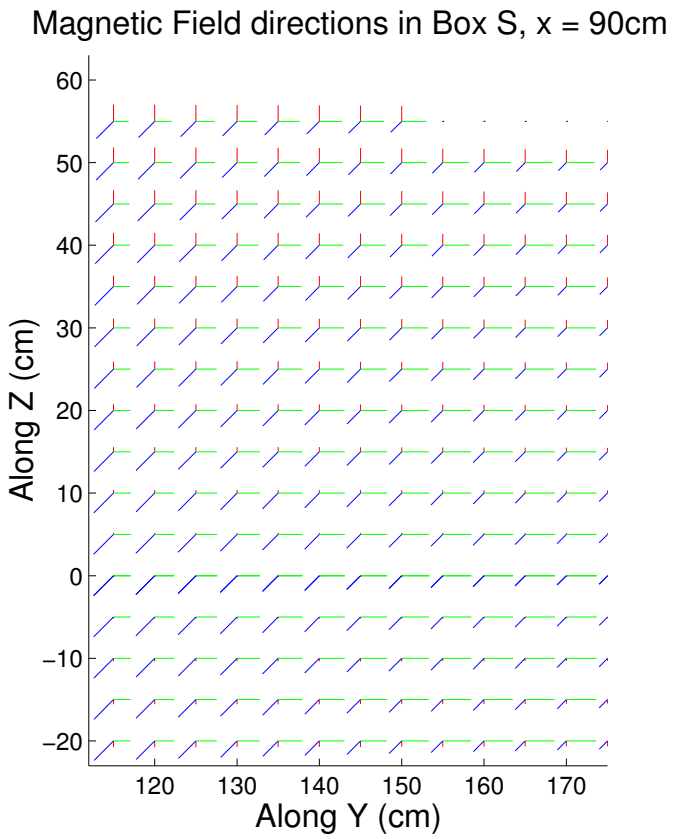


Figure 4-11: The magnetic field directions in the x =90cm plane in AMS coordinates. Magnetic field strengths are normalized.

### 4.3.2 Pressure sensors

The pressure sensors in Box S monitor the pressure in the high pressure Xe and $CO_2$ vessels, which is a NASA safety requirement, as well as monitor the mixing vessel D. The pressure in the Xe and the $CO_2$ tanks is highly dependent on the temperature of the vessels as shown in Fig. 4-12. The gas left in the tanks can be calculated using the Peng-Robinson formula, knowing the temperature and pressure of the vessels. If the tanks get too cold during some high inclination orbit, the pressure does not provide any information about the gas density. The valves can not operate below $0^oC$ either. A thermal model of Box S indicates that the temperatures in Box S will occasionally fall under $0^oC$. Heaters are foreseen to heat up the vessels and the valves to allow Box S to stay operational even through these cold periods.

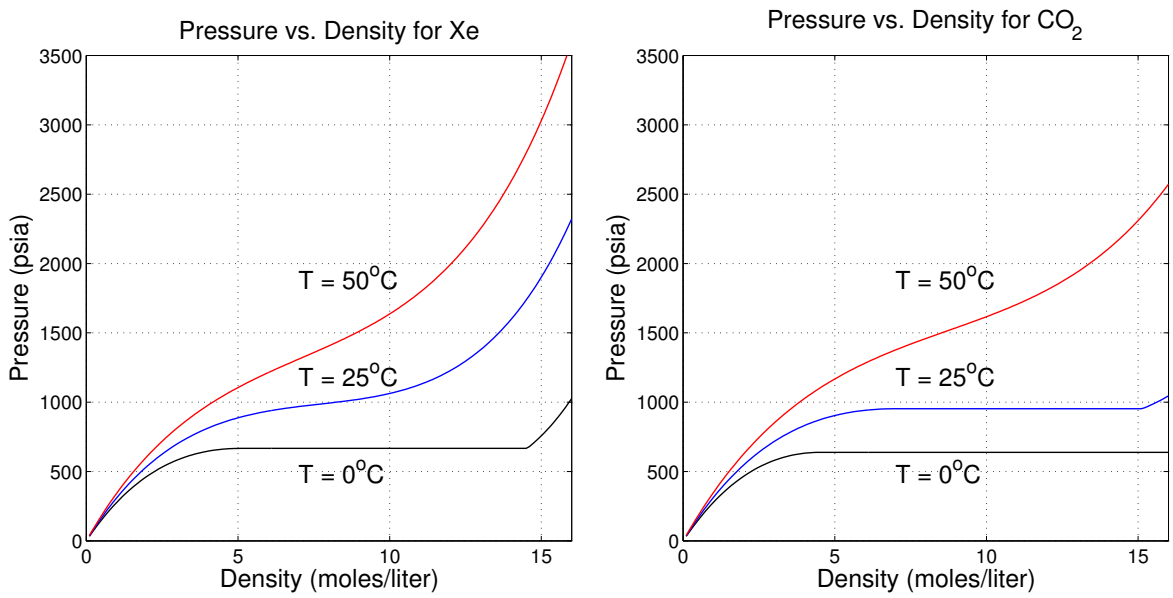


Figure 4-12: The pressure in the gas supply vessels for Xenon and for $CO_2$ as a function of density, using the Peng-Robinson formula, [104]. The critical temperature and pressure data can be found in [89, 16].

The pressure sensors in the TRD gas system have to function under space conditions, a large range of temperatures and pressures and be safe during the operational lifetime. To achieve the mixing accuracy goal, light weight, temperature compensated pressure sensors, with .15% accuracy from GP:50, [70] were chosen. The pressure sensor is shown in Fig. 4-13(b). There are three types, with scales of 25 psi for Box C, 300 psi and 3000 psi for Box S. These sensors were chosen especially for their temperature compensation for non-linearities in its electronics in the -20$^o$C to 65$^o$C regime. A first version of the GP:50 sensors used 24V input with a voltage converter inside it. This version stopped working if the magnetic field reached 500 Gauss. A second version pressure sensor which will be used in flight feeds on a 12V input and consumes 14.8mA maximum power. It is less sensitive to magnetic fields. The pressure head has a slight sensitivity, which can reach 2% at 400 Gauss under certain magnetic field orientations. This sensitivity will be calibrated out in situ. However, they do not fail up to magnetic fields of 1 kGauss. For further redundancy, Kulite pressure sensors, [86], in the flight module will be used. These pressure sensors are not temperature

compensated but are not effected by magnetic fields, and will measure the two vessel high pressure mixing vessel pressures and the mixing vessel pressure.

GP:50 pressure sensors have gone through significant acceptance testing at the company and at MIT. At the company, the pressure sensor was thermally cycled 8 times between -55$^o$ and 125$^o$C while they were not activated, after an electronic burn-in of 150 hours and the initial calibration. One pressure sensor was vibrated at RWTH Aachen I to 10.2 Grms. GP:50 has done their own testing of a pressure sensor head and tested it to 17.1 Grms. By NASA standards, these pressure sensors are "line items" and therefore, have to survive pressures of 4$\times$ MDP(Maximum Design Pressure). This has been shown by calculation by GP:50 as part of the Acceptance Test Procedure, [69]. Also, a hydraulic pressure test at MIT was done on a 3000 psi module to 14000 psi and it held this pressure and did not develop any leaks. The pressure sensor head is hermetically sealed and the electronics cylinder is not. The electronics inside the pressure sensor is conformally coated, which does not let it spark under low pressure conditions. This was tested by a vacuum test overnight to check if any sparking occurred. None was recorded. The temperature compensation test was performed by comparing one temperature sensor at room temperature and one at -20$^o$C, 0$^o$C and at 65$^o$C in a bath. The full scale of the pressure range was tested once thermal equilibrium was reached with the bath. The accuracy of .15% was achieved under all these conditions.

### 4.3.3 Valves

The valves in the TRD gas system were chosen because of their hermetic enclosure and because they do not leak. The Marotta [93] valves of choice, MV197s as seen in Fig. 4-13(a), can open and close thousands of times before failing. They are rated for a operational pressures of $100 - 7000$ psig and have a burst pressure of 25000 psig. The minimum valve opening time is $20msec$. The optimal voltage with which they open is 28V and the inductance is 100 mH.

Box C uses MV100 valves which are slightly different. MV100s were also chosen for Box S initially because it has a mechanical valve status indicator, although it is


Figure 4-13: a) A Marotta MV197 valve. b) A GP:50 pressure sensor in a high pressure holder.

not hermetically sealed and could develop small leaks. In case a valve failed open, the mechanical valve status information would be very valuable. Extensive testing showed that valves do not fail open and so hermeticity was preferred for the high pressure Box S where a small leak can mean a large gas loss. The MV197 valves do not have this valve status indicator. They do not fail open, but they can fail closed. A valve fails closed if it does not open when commanded to do so. However, if a valve does not open, gas will not be transfered. Monitoring the pressure increase in Vessel-D provides information about the status of the valves. The Box-S prototype at MIT has MV100 valves, but the engineering and flight Box-S have MV197 valves.

The MV197s have gone under endurance testing under $0^oC$, $24^oC$, $60^oC$ for 10000 cycles with 500 psi, 1000 cycles with 1500 psi and 100 cycles at 3000 psi and they did not develop leaks or fail open, [49]. They should not operate below $0^oC$ because the Vespel valve seat will not tighten under such conditions. They were put under

| Restrictor name | Location | Restriction |
|---|---|---|
| 01a | Xe branch | 17.6 and 16.8 LkΩ |
| 01b | $CO_2$ branch | 2 x 80.0 LkΩ |
| O2a | Xe:$CO_2$ mixture | 2 x 11.4 LkΩ |
| O2b | Xe:$CO_2$ mixture | 2 x 11.4 LkΩ |

Table 4.1: The flow restrictors in Box S.

3 different orientations in the B field, 0, 45 and 90 degrees to various B fields. The valves have only failed open under certain magnetic field strength and orientation. Testing has shown that if the B field is perpendicular to the axis of symmetry then it never fails open up to fields of 1 kGauss. They have been placed perpendicular to the field where the field is supposed to be highest, at 450G, providing a safety margin of greater than factor of 2.

### 4.3.4 Flow restrictors

The mixing accuracy in Vessel D is achieved by accurate metering of the gas through the flow restrictors on both branches. Since the $CO_2$ content, being less, needs to be very accurate, time constant for that branch has been chosen to be longer. Box S will vent the Vessel D contents slowly through a flow restrictor, O2a or O2b, to Box C to avoid a high pressure gradient that travels through the tubes. The controlled opening time of the valves will allow the mixing program to accurately calculate the amount of gas transfered.

The flow restrictors in Box S are manufactured by the Lee Company, [117] and are viscojets which provides a reasonable degree of viscosity compensation without any moving parts. The viscojets are calibrated in units of Liquid Ohms or Lohms. The restriction of the viscojets are listed in Table 4.3.4. Two Lee restrictors are used in parallel to assure that gas will flow even if one clogs. There are also filters in front of the flow restrictors in the flow diagram as seen in Fig. 4-4. Putting two restrictors in parallel halves the flow restriction. The Lee flow restrictors were placed into cylindrical housings and welded by Arde, [14].

The flow is sonic if the $P_1/P_2 > 1.9$ where $P_1$ is the absolute upstream pressure

| Gas | K (Lohms psi liters/min ) |
|---|---|
| $N_2$ | 275.6 |
| Ar | 244.8 |
| $CO_2$ | 212.8 |
| Xe | 165±20 |

Table 4.2: The gas units constant for various gases at 70$^o$F from [117]. The Xenon value was measured by Reyco Henning.

and $P_2$ is the absolute downstream pressure. In this sonic regime, the gas flow rate, $Q$, can easily be calculated using the following flow equation:

$$Lohms = \frac{K f_T P_1}{Q} \tag{4.1}$$

where K is the "gas units constant", $f_T$ is the "temperature correction factor." If the flow is sub-sonic, then the flow equation becomes:

$$Lohms = \frac{2K f_T \sqrt{\Delta P P_2}}{Q} \tag{4.2}$$

where $\Delta P = P_1 - P_2$. The gas units constant of common and relevant gases are listed in Table 4.2. The sub-sonic flow is slow by definition and applies seldom. The flow that transfers most of the gas is sonic.

The flow restrictors in the engineering Box-S and C were tested using different gases, $N_2$, $CO_2$ and Ar at the integration at CERN. The test results are shown in Fig. 4-14. The measured values are sufficiently close to what is predicted by the restriction and can be used. This confirms the integrity of the housing and welding of the flow restrictors.

### 4.3.5 Functional and vibration testing

After the full engineering Box S was assembled at CERN, it went under leak tests and also functional tests of the valves and the pressure sensors. Then the engineering Box S went under vibration testing in all three directions at Cassacia, Italy to ensure the mechanical integrity of the system. The first vibrational mode is greater than

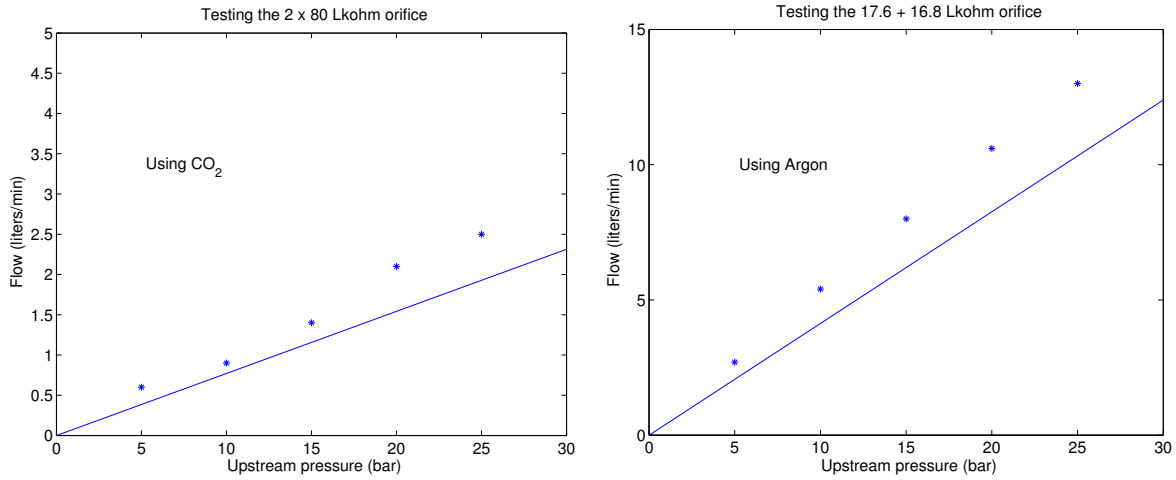


Figure 4-14: Measurements of the flow rates with the flow restrictors used in the Engineering Box S. The lines are predictions.

60 Hz as required by NASA. No leaks developed during the vibration testing of the system. Some mixing cycles which transfer 100 psi of gas into Vessel D were performed by opening valves by hand, using a pre-defined mixing scheme, during the Box S vibration tests. The mixing cycles were performed after each vibration test in different directions to check that the system performance was stable, [43]. Several of these mixing cycles are shown in Fig. 4-15. There was no significant change in the performance of Box S. In one mixing cycle, $CO_2$ is first filled to 20% of the desired mixing ratio and later the mixture is topped off with Argon, instead of Xenon. Each mixing cycle is defined as opening 3 valves on each branch, V1, V2 and V3 to let gas into vessel D. The automated flight mixing method will be discussed in detail in the next section.

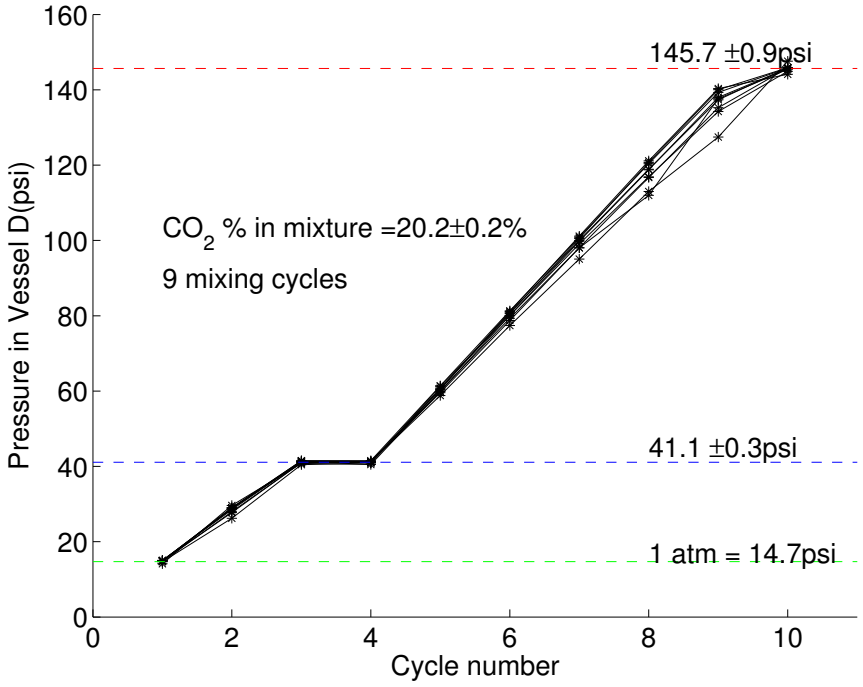


Figure 4-15: Several mixing cycles done by hand after each vibration test on the engineering Box S.

# Chapter 5

# TRD Gas System Electronics and Slow Control

## 5.1 Functional demands

The TRD Gas system electronics will be under the automated control of the main AMS computer during normal operations in space. Intervention from ground should only happen during emergencies, or at system initialization or calibration. The electronics will control and readout Box S, Box C and the manifolds.

For Box S, ignoring the Joule-Thompson effect, the pressure in vessel D will increase from an initial value $P_i$ to a final $P_f$ like

$$P(t) = P_i + (P_f - P_i)(1 - e^{-\frac{t}{R_c V_c}}) \tag{5.1}$$

where $R_c$ is the flow resistance provided by the orifices, $V_c$ the combined volume, dominated by the D vessel. Metering intercepts when P(t) reaches the desired partial pressure. The time for opening the V3 valves on each branch can be pre-calculated either by the using the formula above or by calibrating the mixing to $R_c V_c$ in situ.

The gas system should be able to mix gas accurate enough to meet the 3% gas-gain variation benchmark for the TRD. The TRD at times will need different gas mixtures to maintain the stability of the gas gain, [58]. Since $CO_2$ diffusion is higher

than the Xenon diffusion, it is expected that the $CO_2$ mixing ratio will be higher than 20% to compensate for the loss.

## 5.2 Electronic Implementation

The AMS TRD Gas system will be controlled in space by electronics cards that are fully redundant and radiation-hard, [23]. They operate with low power, and function between 0 and 40$^o$C and survive periods of -40 to 65$^o$C. They have been designed under a tight weight budget of 12kg, excluding cables. They have protection against destructive "latch-up" when crossed by a highly ionizing particle. Each card is conformally coated to prevent arcs at low pressure and is vibration tested to ensure that they will survive launch. All cards will be housed in the UG[1] crate. The system will include a PDB (Power Distribution Box), which provides voltage and current to the UG crate cards and gas system from ISS's supply of 28 VDC. DC-DC converters are needed for 24V, 12V, 5.0V and 3.3V for different applications. The flight UG crate will consume 103W of power. All electronics have to operate in the fringe field of the AMS magnet, of approximately 200Gauss.

To handle the slow control in every sub-detector in AMS in a uniform manner, USCM (Universal Slow Control Module) has been designed by RWTH Aachen III, [105]. All USCMs will be connected to the Monitor and Control Computer and main data acquisition via the CAN-BUS, [41]. A unique ID number is used to address a specific USCM as part of the CAN-protocol. The TRD Gas system has two redundant USCMs. The USCM talks to the gas system control electronics via a custom bus, the LVDS bus, using the LeCroy protocol. The USCM is based on a DS80C390 processor, similar to an 8051. It can issue emergency commands to the control cards autonomously, for example to vent gas in case of an overpressure, but complex commands - like computing partial pressures - are done by the main AMS computer, JMDC, as seen in Fig. 5-1.

The main data computer contains the monitor program, which tests the status

[1]UG stands for the German word for Transition Radiation, *Ubergangstrahlung*.

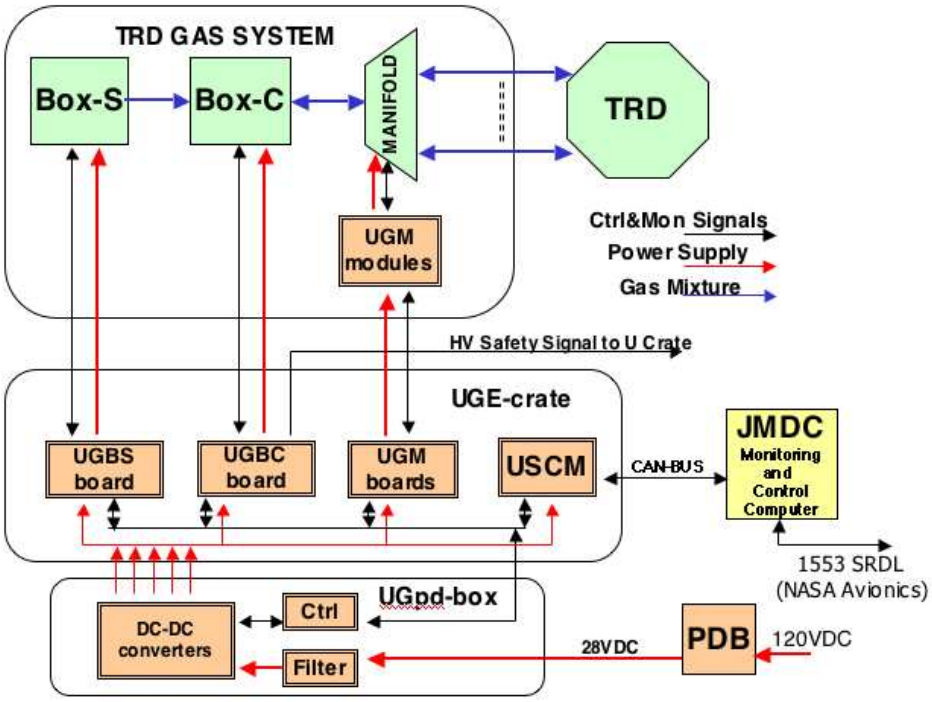


Figure 5-1: The control flow schematic.

information of the gas system against pre-conditions and executes commands. The main computer is one of four redundant PowerPC 750 machines. To minimize the reliance on ground communications, the computer will run a semi-autonomous program (e.g., executing the steps of gas mixture), but will not make operational decisions (e.g. when and whether a gas vent is needed).

The circuit boards UGBS, UGBC, UGFV and UGM provide the electronic interface between USCM and electro-mechanical gas system devices and they have been designed by INFN Roma. These slow control cards have high-power transistors which drive the valves and the pumps and ADCs for the pressure sensors. They relay the serial bus lines and the Dallas temperature sensor, DS1820 [94], bus lines to the USCM for readout. Each card uses an A54SX32A FPGA (Field Programmable Gate Array), which is a finite state machine, as its processor. They are:

1. UGBS controls the valves and the heaters in Box S, and monitors the pressure and the temperature and also the filling status. It will shut down the gas system safely in case of a power or a communications failure. Default state is having

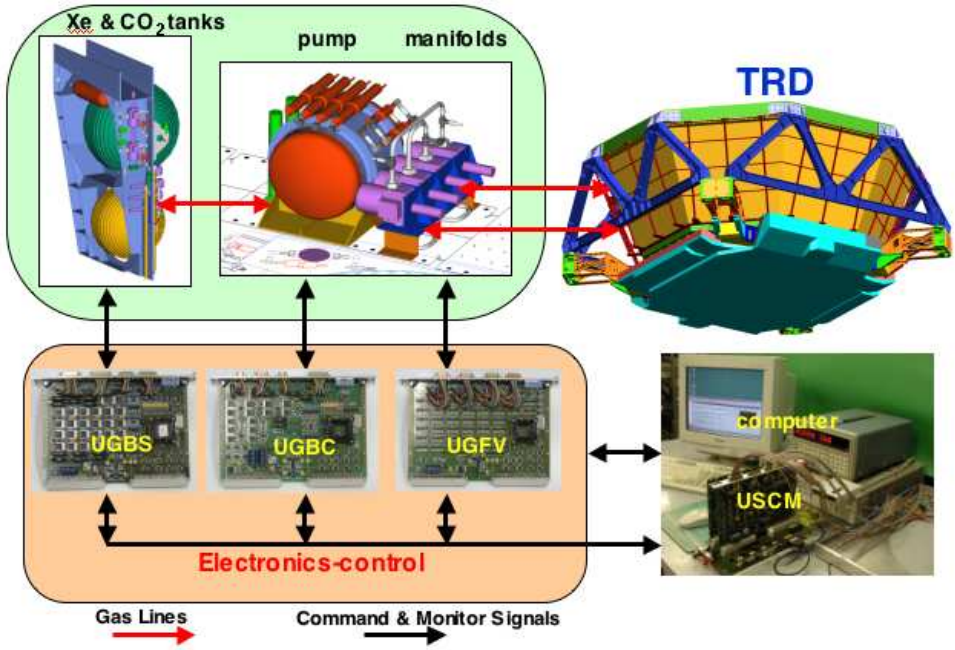


Figure 5-2: Control flow chart showing existing engineering cards.

all valves closed.

2. UGBC controls the circulation pumps, and controls the filling and the venting valves, and runs communications lines to the monitor tube amplifiers, the MCA, and the $CO_2$ analyzer.

3. UGFV monitors the pressure/temperature in each TRD segment. It controls the flow of gas through the TRD modules and can isolate any leaking segments.

4. UGM cards, mounted on the manifolds, pre-amplify the pressure transducer signals.

5. UGHV supplies HV to the calibration tubes in Box-C.

Redundant cables that run to the gas system hardware from the corresponding card's front end provide the electro-mechanical control. The cables have been chosen to have different pin numbers to avoid mixup at integration. All the cards sit in an electronics crate, UG crate, with a backplane which carries all of the power and bus

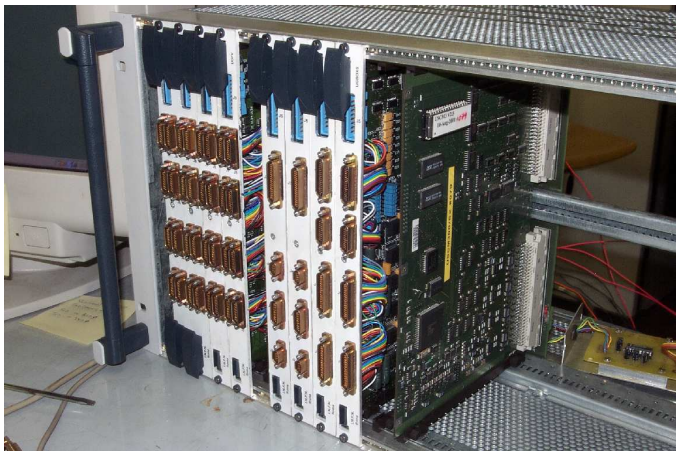

Figure 5-3: The engineering electronics crate. From the left to the right, 4 UGFV, 2 UGBC, 2 UGBS and 1 USCM cards. The engineering USCM does not have a front panel connector.

lines as seen in Fig. 5-3. Each electronics card connect to the backplane through VME slots.

The electronics crate will contain 13 cards in flight: 2 UGBSs, 2 UGBCs, 4 UGFV, 1 UHVG, 2 USCMs. The two halves of UHVG are redundant. In each redundant case, one card is kept "hot" (live and operational) and one "cold" (spare, powered down). The main computer can determine whether any "hot" card has malfunctioned, and can activate the "cold" card.

## 5.3 Slow Control Programming

The engineering UGBS and the engineering USCM has been used as a test-bed to establish the communication protocols for the gas system. The prototype Box-S has been under the control of the UGBS-USCM-computer chain at MIT, as shown in Fig. 5-4. The electro-mechanical connection is provided through the connectors on the front panel of the UGBS. The flight UGBS pin-out for this connector is given in Appendix B. RWTH Aachen III has provided a preliminary USCM backplane, with two slots. Through this backplane, a USCM and a UGBS can communicate the same way they will in the flight crate, through the LeCroy protocol.

The computer controls the USCM using the CAN protocol, through an interface written by RWTH Aachen III, called *can_pc*, [105]. In flight, the JMDC will speak natively in CAN using a PC ISA-bus card. All the USCMs in AMS will sit on the same CAN line. The CAN protocol allows the user to choose which USCM to issue to commands to.

In the USCM-UGBS only testbed, the computer speaks only to one USCM. The *can_pc* interface works on a generic PC and can communicate with the USCM through a custom made EPPCAN Box. This program can be compiled on several operating systems, including Linux and Windows using a C compiler. The EPPCAN Box is connected to the PC's parallel port through an EPP cable. The connection from the EPPCAN Box to the USCM can be either through the USCM backplane or through the USCM front-panel. In our case, USCM front-panel connection is used. The CAN interface like the USCM itself, has two independent CAN channels, A and B for redundancy. The *can_pc* program lets the user issue commands by typing them interactively into a command line prompt or alternatively issue them from a command script file. The user also has access to the monitoring program that runs on the USCM through a serial interface.

These two cards communicate using the LeCroy protocol, which uses the LVDS lines in the backplane. In the flight crate, the LVDS lines will connect all the cards to the USCMs. The communication requires using two lines: ClockLine and DataLine. Each card in the crate is pre-programmed to listen only a specific DataLine and a specific ClockLine. For example, the "hot" UGBS listens on ClockLine 1 and DataLine 1. There is a command under *can_pc* which lets the user issue LeCroy commands. This command takes three arguments, namely the DataLine, the ClockLine and Content. The USCM drives the ClockLine and DataLine for the first 32 bits for the "send" cycle. The USCM continues driving the the ClockLine and the slave card replies by sending bits on the DataLine for the next 32 bits, in the "reply" cycle. The Content sent is the 32-bit command that is assembled according to the structure in Table 5.1 and input as hexadecimal. The Reply that is sent back is also 32-bits and the *can_pc* program outputs this reply in hexadecimal. If there was no reply, the DataLine stays

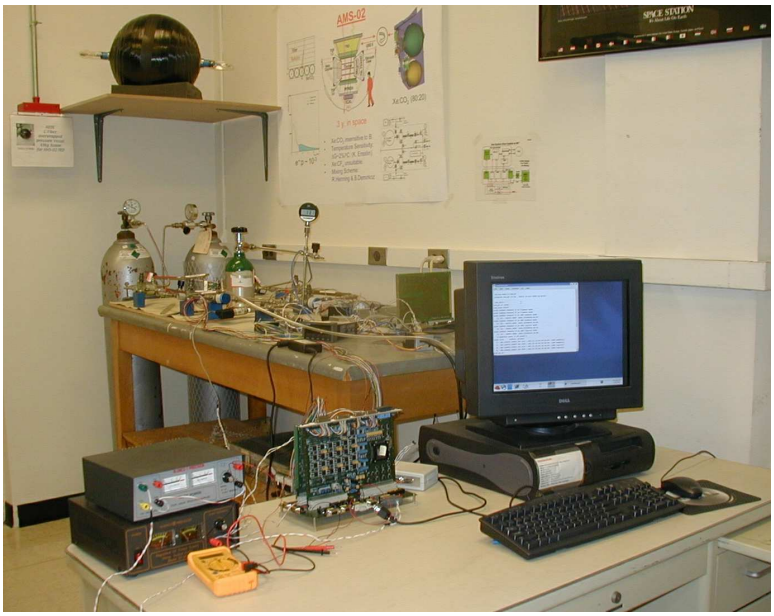


Figure 5-4: The prototype Box S and control system with an engineering USCM and a UGBS at MIT.

in its "default" state and the reply is *0xffffffff*.

Table 5.1: Le Croy command structure

| | | | |
|---|---|---|---|
| S(1) | lead bit = 1 | S(33) | =0 |
| S(2) | Parity bit (odd) | S(34) | echo of S(2) |
| S(3) | "Power Down" Bit | S(35) | echo of S(3) |
| S(4) | Broadcast Bit | S(36) | echo of S(4) |
| S(5:12) | Select Code, address | S(37:44) | echo of S(5:12) |
| S(13) | Read/Write bit | S(45) | echo of S(13) |
| S(14:16) | Section Address | S(46:48) | echo of S(14:16) |
| S(17:32) | Data to be written | S(49:64) | Data to be read |

The USCM sends the Content to all the cards that are listening on a particular ClockLine and DataLine. The distinction between different cards is made in the Content of the LeCroy message. For example, the "hot" UGBS and the "hot" UGBC will be listening on the same DataLine and ClockLine but the *Board Address* which is defined as bits (10:12) of the LeCroy protocol will distinguish between the cards. All the commands for the UG-crate have been defined using 5-bits, (5:9). The list of

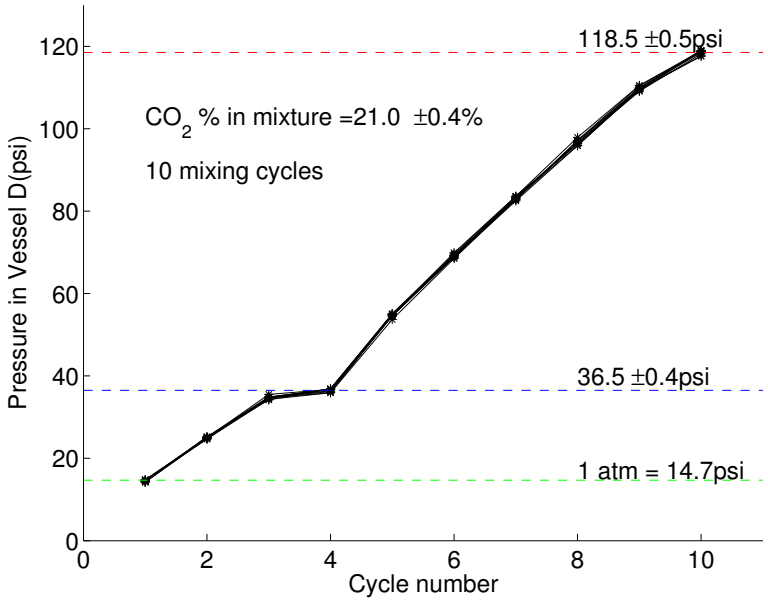


Figure 5-5: 10 mixing cycles with Ar and $CO_2$ using the Box S prototype at MIT.

available commands which are part of the Select Code of the protocol are listed for each engineering card in Appendix A. There might be some changes in the command table for the flight cards, corresponding to mechanical changes made in the gas system since the first versions. For purposes of the UG-crate, the "Power Down" and the "Broadcast" bit are not used and been defined to be always 0. The "Section Address" is used to refer to different modules controlled by the UHVG cards but otherwise not used and set to 0. The "Read/Write" bit in the LeCroy protocol has a misleading name. The USCM always *writes* and never *just reads*. If the USCM is issuing a command that will change the state of the card, we call this "Write" and if the USCM is issuing a command to ask for some state of some valve or wants to know some ADC value, we call this "Read." The bit is set to 1 if the USCM has issued a Write command. Some commands can only be issued as a Write and some as a Read and some can be either. Data may be written under the Write mode and depending on the command that was issued can be valve opening times or which ADC line to read. The Write or Read mode is indicated in parenthesis in the tables in Appendix A as well as the number of Data bits that relates to that command if relevant.

The USCM-UGBS testbed at MIT has been used to issue commands to the UGBS

and debug the hardware and software interface. Code has been added to the *can_pc* program as a low level interface to the UGBS. For example, issuing *ugas V1a 10* under the *can_pc* program, will let the user open the valve V1a for 10 seconds. Using the scripting feature of the *can_pc* program, a mixing script was written, by specifying valves to open for certain periods of time and reading the pressure sensors to determine the mixture. Such a script can be run by only typing one command, namely the script name. The mixing script which was repeated 10 times shows that the mixing accuracy can be as good as 0.4% as shown in Fig. 5-5.

# Chapter 6

# Conclusions

The TRD gas supply system and the slow control for it has been designed to allow for the required accuracy of the TRD gas parameters. In the harsh space environment, it is expected to provide gas in a well balanced mixture for at least three years. The design is redundant, light-weight and consumes very little power.

The TRD has been designed with the physics goals in mind, to be as efficient as possible with the transition radiation photon detection and achieve a stable calibrated separation. Mechanically it is being gas-tight, structurally accurate and light-weight.

The cosmic ray spectrum will be explored, in space for the first time, by high statistics at large energies in pursuit of dark matter and antimatter.

# Appendix A

# Gas System Slow Control Commands

Table A.1: Engineering Manifolds commands

| S(9:5) | Device |
|---|---|
| 00000 | Reserved |
| 00001 | Open/Close On Module 1 (16 bit W) |
| 00010 | Open/Close On Module 2 (16 bit W) |
| 00011 | Open/Close On Module 3 (16 bit W) |
| 00100 | Open/Close On Module 4 (16 bit W) |
| 00101 | Open/Close On Module 5 (16 bit W) |
| 00110 | Open/Close On Module 6 (16 bit W) |
| 00111 | Open/Close On Module 7 (16 bit W) |
| 01000 | Open/Close On Module 8 (16 bit W) |
| 01001 | Open/Close All Modules (16 bit W) |
| 01010 | Reserved |
| 01011 | Reserved |
| 01100 | Reserved |
| 01101 | Reserved |
| 01110 | Reserved |
| 01111 | HV Safety Signal (4bitW, 2bitR) |
| 10000 | Select on ADC Mux lines (15 bit RW) |
| 10001 | Reserved |
| 10010 | Regulators Register (4bitR, 1bitW) |

Table A.2: Engineering Box S commands

| S(9:5) | Device |
|---|---|
| 00000 | Reserved |
| 00001 | MV100 Enable Register (13 bit , RW) |
| 00010 | Electrical Current SR (13 bit , R) |
| 00011 | Mechanical Open Current SR (13 bit, R) |
| 00100 | Mechanical Close Current SR (13 bit,R) |
| 00101 | Electrical Event SR (13 bit , R) |
| 00110 | Mechanical Open Event SR (13 bit, R) |
| 00111 | Mechanical Close Event SR (13 bit, R) |
| 01000 | Open Valve V1a (16 bit, W) |
| 01001 | Open Valve V2a (16 bit, W) |
| 01010 | Open Valve V3a (16 bit, W) |
| 01011 | Open Valve V4a (16 bit, W) |
| 01100 | Open Valve V5 (16 bit, W) |
| 01101 | Open Valve V10a (16 bit, W) |
| 01110 | Open Valve V20a (16 bit, W) |
| 01111 | Open Valve V1b (16 bit, W) |
| 10000 | Open Valve V2b (16 bit, W) |
| 10001 | Open Valve V3b (16 bit, W) |
| 10010 | Open Valve V4b (16 bit, W) |
| 10011 | Open Valve V10b (16 bit, W) |
| 10100 | Open Valve V20b (16 bit, W) |
| 10101 | Open Valve V20a&V20b (16 bit, W) |
| 10110 | Read P1a values (12 bit, R) |
| 10111 | Read T1a values (12 bit, R) |
| 11000 | Read P1b values (12 bit, R) |
| 11001 | Read T1b values (12 bit, R) |
| 11010 | Read P2a values (12 bit, R) |
| 11011 | Read T2a values (12 bit, R) |
| 11100 | Read P2b values (12 bit, R) |
| 11101 | Read T2b values (12 bit,R) |
| 11110 | Regulators Register (2 bit, RW) |

Table A.3: Engineering Box C commands

| S(9:5) | Device |
|---|---|
| 00000 | Reserved |
| 00001 | MV100 Enable Register (4 bit, RW) |
| 00010 | Pump Speed & Enable Register (4 bit, RW) |
| 00011 | MCA Select Register (4 bit, RW) |
| 00100 | Current Status Register ((16 bit, R) |
| 00101 | Event Status Register (12 bit, RW) |
| 00110 | Open Valve V6a (16 bit, W) |
| 00111 | Open Valve V6b (16 bit, W) |
| 01000 | Open Valve V18a (16 bit, W) |
| 01001 | Open Valve V18b (16 bit, W) |
| 01010 | Open Valve V6a and V18a (16 bit, W) |
| 01011 | Open Valve V6b and V18b (16 bit, W) |
| 01100 | Open/Close Valve V8a (16 bit, W) |
| 01101 | Open/Close Valve V8b (16 bit, W) |
| 01110 | Run/Stop Pump P1 (1 bit, W) |
| 01111 | Run/Stop Pump P2 (1 bit, W) |
| 10000 | Activate HV Safety Signal (? bit, W) |
| 10001 | Read P4 values (12 bit, R) |
| 10010 | Read T4 values (12 bit, R) |
| 10011 | Read P5 values (12 bit, R) |
| 10100 | Read T5 values (12 bit, R) |
| 10101 | Read P6 values (12 bit, R) |
| 10110 | Read T6 values (12 bit, R) |
| 10111 | Read CP1 curr (12 bit, R) |
| 11000 | Read CP2 curr (12 bit, R) |
| 11001 | RS232 register (4 bit, RW) |
| 11010 | Regulators Register (3bit, RW) |

# Appendix B

# Box-S Pinout

Here we document the pinout for the control of Box S. Glenair Micro-D connectors that conform to MIL-PRF-83513 with different number of pins are used: 37 pin, 31 pin and 21 pin to avoid mixup. The 37 pin connector is the most important from a safety stand point since it controls the valves. Hence it is redundant. Mechanically, there is 0.050 inch contact spacing and 0.043 inch spacing between rows. The first pin is marked on the connector as "1." The mechanical arrangement for the mating face of the pin connector is shown in Figure B-1. The mating face of the socket connector is a mirror image of this arrangement, [68].

For the functional placement of the pins, the supply voltages have been bunched up together. For example, positive excitation (+24V) for the 37pin connector are all bunched up together and there is a row of unconnected pins between them and the negative excitation pins. Same is true for the heaters. On the 21pin connector, the readout pins for each sensor is also grouped to allow easier cable routing.

On Box S, a pre-wired and fully potted pigtail harness is used. The pigtail ends are soldered to the valves, temperature and pressure sensors and heaters as listed on Table B.1.

Table B.1: Box S pinout

| **JS1A&JS1B (37pin)** | | **JS2 (21pin)** | | **JS3 (31pin)** | |
|---|---|---|---|---|---|
| Pin # | Connection | Pin # | Connection | Pin # | Connection |
| 1 | V1A +E | 1 | Kulite 1 +E | 1 | Heater 1 +E |
| 2 | V10A +E | 2 | Kulite 2 +E | 2 | Heater 2 +E |
| 3 | V3A +E | 3 | unconnected | 3 | Heater 3 +E |
| 4 | V20B +E | 4 | Kulite 1 -E | 4 | Heater 4 +E |
| 5 | V3B +E | 5 | Kulite 2 -E | 5 | Heater 5 +E |
| 6 | V4A +E | 6 | Kulite 1 SR | 6 | Heater 1 -E |
| 7 | unconnected | 7 | Kulite 2 SR | 7 | Heater 2 -E |
| 8 | V1A -E | 8 | Kulite 3 SR | 8 | Heater 3 -E |
| 9 | V10A -E | 9 | Dallas 1 IO | 9 | Heater 4 -E |
| 10 | V3A -E | 10 | Dallas 2 GND | 10 | Heater 5 -E |
| 11 | V20B -E | 11 | Dallas 2 VCC | 11 | P1A SR |
| 12 | V3B -E | 12 | Kulite 3 +E | 12 | P1B P |
| 13 | V4A -E | 13 | unconnected | 13 | P1B T |
| 14 | unconnected | 14 | unconnected | 14 | P2A SR |
| 15 | P1A -E | 15 | Kulite 3 -E | 15 | P2B P |
| 16 | P1B -E | 16 | Kulite 1 P | 16 | P2B T |
| 17 | unconnected | 17 | Kulite 2 P | 17 | Heater 6 +E |
| 18 | P1A +E | 18 | Kulite 3 P | 18 | Heater 7 +E |
| 19 | P1B +E | 19 | Dallas 1 GND | 19 | Heater 8 +E |
| 20 | V20A +E | 20 | Dallas 1 VCC | 20 | Heater 9 +E |
| 21 | V2A +E | 21 | Dallas 2 IO | 21 | unconnected |
| 22 | V1B +E | | | 22 | Heater 6 -E |
| 23 | V10B +E | | | 23 | Heater 7 -E |
| 24 | V2B +E | | | 24 | Heater 8 -E |
| 25 | V4B +E | | | 25 | Heater 9 -E |
| 26 | unconnected | | | 26 | P1A P |
| 27 | V20A -E | | | 27 | P1A T |
| 28 | V2A -E | | | 28 | P1B SR |
| 29 | V1B -E | | | 29 | P2A P |
| 30 | V10B -E | | | 30 | P2A T |
| 31 | V2B -E | | | 31 | P2B SR |
| 32 | V4B -E | | | | |
| 33 | P2A -E | | | | |
| 34 | P2B -E | | | | |
| 35 | unconnected | | | | |
| 36 | P2A +E | | | | |
| 37 | P2B +E | | | | |

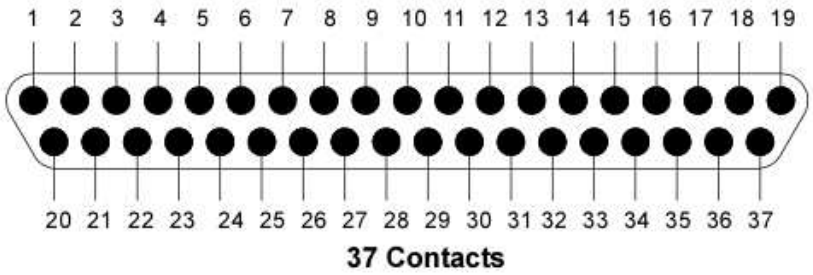


Figure B-1: The mechanical arrangement of the mating face of a Glenair 37 pin connector, [68].

# Bibliography


[1] M. Acciarri et al. Search for charginos and neutralinos in e+ e- collisions at s**(1/2) = 189-GeV. *Phys. Lett.*, B472:420–433, 2000.

[2] F. C. Adams et al. Constraints on the intergalactic transport of cosmic rays. *Astrophys. J.*, 491:6–12, 1997.

[3] M. Aguilar et al. A study of cosmic ray secondaries induced by the MIR space station using AMS-01. 2004. submitted to *Nucl. Instrum. Meth. B*.

[4] T. Akesson et al. Straw tube drift-time properties and electronics parameters for the ATLAS TRT detector. *Nucl. Instrum. Meth.*, A449:446–460, 2000.

[5] J. Alcaraz et al. Search for antihelium in cosmic rays. *Phys. Lett.*, B461:387–396, 1999.

[6] J. Alcaraz et al. Cosmic protons. *Phys. Lett.*, B490:27–35, 2000.

[7] J. Alcaraz et al. Leptons in near earth orbit. *Phys. Lett.*, B484:10–22, 2000.

[8] J. Alcaraz et al. Protons in near earth orbit. *Phys. Lett.*, B472:215–226, 2000.

[9] B. Alpat. Alpha Magnetic Spectrometer (AMS02) experiment on the International Space Station (ISS). 2003. astro-ph/0308487.

[10] M. Ambriola. Performance of the transition radiation detector of the PAMELA space mission. *Nucl. Phys. Proc. Suppl.*, 113:322–328, 2002.

[11] M. Ambriola et al. Supervised algorithms for particle classification by a transition radiation detector. *Nucl. Instrum. Meth.*, A510:362–370, 2003.

[12] M. Ambrosio et al. Measurement of the energy spectrum of underground muons at Gran Sasso with a transition radiation detector. *Astropart. Phys.*, 10:11–20, 1999.

[13] H. Anderhub et al. Design and construction of the prototype synchrotron radiation detector. *Nucl. Instrum. Meth.*, A491:98–112, 2002.

[14] Arde Inc. http://www.ardeinc.com/four.html.

[15] J. N. Bahcall and E. Waxman. Has the GZK cutoff been discovered? *Phys. Lett.*, B556:1–6, 2003.

[16] V. G. Baidakov et al. The equation of state of metastable liquid xenon near the critical point. *Phys. Let. A*, 131:119–121, 1988.

[17] E. A. Baltz and J. Edsjo. Positron propagation and fluxes from neutralino annihilation in the halo. *Phys. Rev.*, D59:023511, 1999.

[18] E. A. Baltz et al. The positron excess and supersymmetric dark matter. 2002. astro-ph/0211239.

[19] F. Barao et al. Cerenkov angle and charge reconstruction with the RICH detector of the AMS experiment. *Nucl. Instrum. Meth.*, A502:310–314, 2003.

[20] E. Barbarito et al. A high rejection transition radiation detector prototype to distinguish positrons from protons in a cosmic ray space laboratory. *Nucl. Instrum. Meth.*, A313:295–302, 1992.

[21] E. Barbarito et al. Straw chambers operating in vacuum for particle tracking and transition radiation detection in accelerator and space experiments. *Nucl. Instrum. Meth.*, A381:39–48, 1996.

[22] A. Barrau. AMS: A particle observatory in space. 2001. astro-ph/0103493.

[23] A. Bartoloni et al. Transition Radiation Detector Gas Slow Control System for AMS-02, 2001. http://ams.cern.ch/AMS/TRDGas/monitoring /TRD-note_v14bis.pdf.

[24] S. W. Barwick et al. Measurements of the cosmic-ray positron fraction from 1-GeV to 50-GeV. *Astrophys. J.*, 482:L191–L194, 1997.

[25] G. Bassompierre et al. Performance of the NOMAD transition radiation detector. *Nucl. Instrum. Meth.*, A411:63–74, 1998.

[26] R. Battiston. The capabilities of the Alpha Magnetic Spectrometer as GeV gamma-rays detector. 1999. astro-ph/9911241.

[27] R. Battiston. Astro particle physics from space. 2002. astro-ph/0208108.

[28] A. S. Beach et al. Measurement of the cosmic-ray antiproton to proton abundance ratio between 4-GeV and 50-GeV. *Phys. Rev. Lett.*, 87:271101, 2001.

[29] R. Beck. Magnetic fields in the Milky Way and other spiral galaxies. 2003. astro-ph/0310287.

[30] R. Becker. TRD Gas System Integration Website, http://rbecker.home.cern.ch /rbecker/tdg.html.

[31] U. Becker et al. TRD Gas system Summary and Specifications, 2003. http:// ams.cern.ch/AMS/TRDGas/TRDGasSummary4April2003.ps.

[32] R. Bellotti et al. A transition radiation detector for positron identification in particle astrophysics experiments. Presented at Int. Cosmic Ray Conf., Calgary, Canada, Jul 19 - 30, 1993.

[33] C. L. Bennett et al. First Year Wilkinson Microwave Anisotropy Probe (WMAP) Observations: Preliminary Maps and Basic Results. *Astrophys. J. Suppl.*, 148:1, 2003.

[34] E. Bertschinger. Dark Matter Caustics. Presented at MIT Astrophysics Internal Symposium, Sept 9-11, 2003.

[35] V. Bindi et al. The AMS-02 time of flight system. Final design. 2003. hep-ex/0305074.

[36] B. Blau et al. The superconducting magnet of AMS-02. *Nucl. Phys. Proc. Suppl.*, 113:125–132, 2002.

[37] W. Blum and L. Rolandi. *Particle Detection with Drift Chambers*. Springer-Verlag, Berlin, Second edition, 1994. p. 1-38, 124-127.

[38] P. Bobik et al. A Complete Simulation of Cosmic Rays Access to a Space Station. Presented at ICATPP-7, Como, Italy, Oct 15 - 19, 2001.

[39] A. Bottino et al. Supersymmetric dark matter. *Nucl. Phys. Proc. Suppl.*, 113:50–59, 2002.

[40] A. Bouchet et al. Simulation of cosmic Be isotopes detected by the RICH in AMS on the ISS. *Nucl. Phys. A*, 688:417–420, 2001.

[41] H. Broeker. USCM Software Flight Plan. http://ams.cern.ch/AMS/Reports/TIMOct03/Broeker_TIM031027.pdf, Presented at the AMS Technical Interchange Meeting, October 2003.

[42] M. Buenerd. The RICH counter of the AMS experiment. *Nucl. Instrum. Meth.*, A502:158–162, 2003.

[43] J. Burger. TRD Gas System. Presented at the AMS Technical Interchange Meeting, CERN, Jan 19, 2004.

[44] J. Burger and B. Demirkoz. AMS-02 TRD Gas System Documents, http://ams.cern.ch/AMS/TRDGas/.

[45] W. J. Burger. The AMS silicon tracker. *Nucl. Phys. Proc. Suppl.*, 113:139–146, 2002.

[46] S. Burles, K. M. Nollett, and M. S. Turner. Big-Bang nucleosynthesis predictions for precision cosmology. *Astrophys. J.*, 552:L1–L6, 2001.

[47] F. Cadoux et al. The AMS-02 electromagnetic calorimeter. *Nucl. Phys. Proc. Suppl.*, 113:159–165, 2002.

[48] F. S. Cafagna. The PAMELA transition radiation detector. Prepared for 26th Int. Cosmic Ray Conf., Salt Lake City, Utah, 17 - 25 Aug 1999.

[49] G. Carosi. Personal communication.

[50] G. Carosi. Positron/Proton Separation using AMS-02 TRD. Presented at SpacePart Conf., Washington DC, Dec 10-12, 2003. Submitted to *Nucl. Phys. B.*

[51] D. Casadei. *Direct measurement of galactic cosmic ray fluxes with the orbital detector AMS-02.* PhD thesis, University of Bologna, 2003.

[52] D. Casadei et al. The AMS-02 time of flight system. *Nucl. Phys. Proc. Suppl.*, 113:133–138, 2002.

[53] CERN Application Software Group: Computing and Networks Division. *GEANT: Detector Description and Simulation Tool.* Geneva, Switzerland, 1993. http://wwwasd.web.cern.ch/wwwasd/.

[54] H.-C. Cheng, J. L. Feng, and K. T. Matchev. Kaluza-Klein dark matter. *Phys. Rev. Lett.*, 89:211301, 2002.

[55] S. Coutu et al. Cosmic-ray positrons: Are there primary sources? *Astropart. Phys.*, 11:429–435, 1999.

[56] R. H. Cyburt et al. Constraining strong baryon dark matter interactions with primordial nucleosynthesis and cosmic rays. *Phys. Rev.*, D65:123503, 2002.

[57] W. de Boer et al. Positron fraction from dark matter annihilation in the CMSSM. *Nucl. Phys. Proc. Suppl.*, 113:221–228, 2002.

[58] B. Demirkoz. Slow Control for the TRD Gas Supply System of AMS-02. Presented at SpacePart Conf., Washington DC, Dec 10-12, 2003. Submitted to *Nucl. Phys. B.*

[59] B. Demirkoz. *Studies of Transition Radiation Detectors for AMS.* Undergraduate thesis, MIT, 2001.

[60] B. Dolgoshein. Transition radiation detectors. *Nucl. Instrum. Meth.*, A326:434–469, 1993.

[61] M. A. DuVernois et al. Cosmic ray electrons and positrons from 1-GeV to 100-GeV: Measurements with HEAT and their interpretation. *Astrophys. J.*, 559:296–303, 2001.

[62] V. Egorychev, V. Saveliev, and S. J. Aplin. Particle identification via transition radiation and detectors. *Nucl. Instrum. Meth.*, A453:346–352, 2000.

[63] J. L. Feng, K. T. Matchev, and F. Wilczek. Particle and astroparticle searches for supersymmetry. *eConf*, C010630:P309, 2001.

[64] P. Fisher and G. Rybka. Personal communication.

[65] Yu V. Galaktionov. Antimatter in cosmic rays. *Rep. Prog. Phys*, 65(9):1243–1270, 2002.

[66] C. Gargiulo. TRD Gas Supply System Vibration Test. http://ams.cern.ch/AMS/Reports/TIMJan04/Box_S_TIM_Jan04.ppt, Presented at the AMS Technical Interchange Meeting, January 2004.

[67] S. Gentile. The Performance of the Transition Radiation Detector of AMS-02 experiment. Presented at the IEEE Conference, Portland, Oregon, 19-25 Oct, 2003.

[68] Glenair Inc. http://www.glenair.com/micro-d/m83513.html.

[69] GP:50. Acceptance Test Procedure for GP:50 Aerospace Division Pressure Transducers Manufactured for MIT. 28th May 2003.

[70] GP:50. http://www.gp50.com/pdf/7900.pdf.

[71] G. E. Graham et al. Design and test results of a transition radiation detector for a Fermilab fixed target rare kaon decay experiment. *Nucl. Instrum. Meth.*, A367:224–227, 1995.

[72] D.E. Groom et al. Review of Particle Physics. *The European Physical Journal*, C15, 2000. URL: http://pdg.lbl.gov.

[73] J. Han. Magnetic fields in our Galaxy: How much do we know? (II) Halo fields and the global field structure. 2001. astro-ph/0110319.

[74] S. Harrison et al. Cryogenic System for a Large Superconducting Magnet in Space. Presented at Applied Superconductivity Conf., Houston, Texas, 2002.

[75] R. Henning. Design and Performance of a Future Space Based Transition Radiation Detector. Presented at the APS DPF Conf., Williamsburg, Virginia, May 24-28, 2002.

[76] R. Henning. *Search for Antideuterons and Strangelets in Cosmic Rays with AMS-01*. PhD thesis, MIT, 2003.

[77] P. Henryk. Transition radiation detector in the D0 colliding beam experiment at Fermilab. Presented at 7th Vienna Wire Chamber Conf., Vienna, Austria, Feb 13-17, 1995.

[78] D. Hooper, J. E. Taylor, and J. Silk. Can supersymmetry naturally explain the positron excess? 2003. hep-ph/0312076.

[79] J. D. Jackson. *Classical Electrodynamics*. John Wiley & Sons, Inc., New York, third edition, 1998. p. 646-654.

[80] G. Jungman, M. Kamionkowski, and K. Griest. Supersymmetric dark matter. *Phys. Rept.*, 267:195–373, 1996.

[81] T. Kirn. Status of AMS TRD. Presented at the AMS Technical Interchange Meeting, Johnson Space Center, Houston, Oct 30, 2002.

[82] T. Kirn. Status of TRD Module Production. Presented at the AMS Technical Interchange Meeting, CERN, Jan 19, 2004.

[83] T. Kirn and T. Siedenburg. The AMS-02 Transition Radiation Detector. Presented at the 10th Vienna Conf. on Instrum., Feb 16-21, 2004. submitted to *Nucl. Instrum. Meth. A*.

[84] E. W. Kolb and M. S. Turner. *The Early Universe*. Frontiers in physics, 1990. p. 157-193.

[85] A. Kounine and V. Koutsenko. AMS-2 TRD uniformity requirements and in-situ calibration. AMS-Note-20-March-2000.

[86] Kulite Semiconductor Products, Inc. http://www.kulite.com.

[87] G. Lamanna. Astrophysics and particle physics in space with the Alpha Magnetic Spectrometer. *Mod. Phys. Lett.*, A18:1951–1966, 2003.

[88] W. R. Leo. *Techniques for Nuclear and Particle Physics Experiments*. Springer-Verlag, Berlin, First edition, 1987. p. 119-133.

[89] D. R. Lide et al. *CRC Handbook of Chemistry and Physics*. CRC Press, LLC, 84th edition, 2003-2004. Fluid properties, critical constants.

[90] C.-P. Ma and E. Bertschinger. A Cosmological Kinetic Theory for the Evolution of Cold Dark Matter Halos with Substructure: Quasi-Linear Theory. 2003. astro-ph/0311049.

[91] P. Maestro. *A study on background rejection and $e^+$ and $\gamma$ detection in AMS 02*. PhD thesis, University of Siena, INFN, 2003. AMS-Note 2003-01-01.

[92] T. Mahmoud. The ALICE transition radiation detector. *Nucl. Instrum. Meth.*, A502:127–132, 2003.

[93] Marotta Controls Inc. http://www.marotta.com.

[94] Maxim Integrated Products. DS1820, DS18S20 Digital Thermometer Replacements. http://www.maxim-ic.com/quick_view2.cfm/qv_pk/3021.

[95] M. N. Mazziotta. Transition radiation detector in MACRO. 1999. hep-ex/9905018.

[96] B. Monreal. Personal communication.

[97] I. V. Moskalenko and A. W. Strong. Positrons from particle dark-matter annihilation in the galactic halo: Propagation Green's functions. *Phys. Rev.*, D60:063003, 1999.

[98] D. Muller et al. Energy spectra and relative abundances of heavy cosmic-ray nuclei around 1-TeV/nucleon. Prepared for 28th Int. Cosmic Ray Conf., Tsukuba, Japan, 31 Jul - 7 Aug 2003.

[99] C. Munoz. Dark matter detection in the light of recent experimental results. 2003. hep-ph/0309346.

[100] J. F. Navarro, C. S. Frenk, and S. D. M. White. The Structure of Cold Dark Matter Halos. *Astrophys. J.*, 462:563–575, 1996.

[101] K. M. Nollett and S. Burles. Estimating reaction rates and uncertainties for primordial nucleosynthesis. *Phys. Rev.*, D61:123505, 2000.

[102] Omega Engineering Inc. http://www.omega.com.

[103] L. Page et al. First Year Wilkinson Microwave Anisotropy Probe (WMAP) Observations: Interpretation of the TT and TE Angular Power Spectrum Peaks. 2003. astro-ph/0302220.

[104] D. Peng and D. Robinson. A new two-constant equation of state. *Ind. Eng. Chem. Fundam.*, 15:59–64, 1976.

[105] RWTH Aachen III. AMS-02 USCM webpage. http://www.physik.rwth-aachen.de/group/IIIphys/Electronics/AMS-II.

[106] A. D. Sakharov. Violation of CP invariance, C asymmetry, and baryon asymmetry of the universe. *Pisma Zh. Eksp. Teor. Fiz.*, 5:32–35, 1967.

[107] T. Sanuki et al. Precise measurement of cosmic-ray proton and helium spectra with the BESS spectrometer. *Astrophys. J.*, 545:1135, 2000.

[108] V. Saveliev. The HERA-B transition radiation detector. *Nucl. Instrum. Meth.*, A408:289–295, 1998.

[109] T. Schael. AMS-02 TRD Status Report. Presented at the AMS Technical Interchange Meeting, CERN, June, 2001.

[110] A. Shirokov. Personal communication.

[111] V. Shoutko, G. Lamanna, and A. Malinin. Cosmic photon and positron spectra measurements modeling with the AMS-02 detector at ISS. *Int. J. Mod. Phys.*, A17:1817–1828, 2002.

[112] T. Siedenburg. TRD Module Production and Beamtests. Presented at the AMS02 TRD Meeting, MIT, Nov 20, 2000.

[113] T. Siedenburg et al. A transition radiation detector for AMS. *Nucl. Phys. Proc. Suppl.*, 113:154–158, 2002.

[114] J. Silk and A. Stebbins. Clumpy cold dark matter. *Astrophys. J.*, 411:439–449, 1993.

[115] Space Cryomagnetics Ltd. http://www.spacecryo.com.

[116] D. N. Spergel et al. First Year Wilkinson Microwave Anisotropy Probe (WMAP) Observations: Determination of Cosmological Parameters. *Astrophys. J. Suppl.*, 148:175, 2003.

[117] The Lee Company. http://www.theleeco.com.

[118] D. M. Thiessen. *The gas system for the HERMES transition radiation detector.* Master's thesis, Simon Fraser University, 1996. DESY-HERMES-96-28.

[119] T. Thuillier et al. Experimental study of a proximity focusing Cerenkov counter prototype for the AMS experiment. *Nucl. Instrum. Meth.*, A491:83–97, 2002.

[120] H. J. Volk. Gamma-ray astronomy of cosmic rays. 2002. astro-ph/0202421.

[121] S. P. Wakely et al. Transition radiation detectors for cosmic rays near the knee. Prepared for 28th Int. Cosmic Ray Conf., Tsukuba, Japan, 31 Jul - 7 Aug 2003.